Noncontact Surface Thermometry for Microsystems: LDRD Final Report

Sean P. Kearney, Justin R. Serrano, Leslie M. Phinney, Samuel Graham, Thomas Beecham, and Mark R. Abel

Approved for public release; further dissemination unlimited.

Sandia National Laboratories

NONCONTACT SURFACE THERMOMETRY FOR MICROSYSTEMS: LDRD FINAL REPORT

Sean P. Kearney
Thermal-Fluid Experimental Sciences Department 1512

Justin R. Serrano and Leslie M. Phinney
Microscale Science and Technology Department 1513

Engineering Sciences Center
Sandia National Laboratories
P.O. Box 5800
Albuquerque, NM 87185-0834

Samuel Graham, Thomas Beecham, and Mark R. Abel
G.W. Woodruff School of Mechanical Engineering
Georgia Institute of Technology
Atlanta, GA 30332

ABSTRACT

We describe a Laboratory Directed Research and Development (LDRD) effort to develop and apply laser-based thermometry diagnostics for obtaining spatially resolved temperature maps on working microelectromechanical systems (MEMS). The goal of the effort was to cultivate diagnostic approaches that could adequately resolve the extremely fine MEMS device features, required no modifications to MEMS device design, and which did not perturb the delicate operation of these extremely small devices. Two optical diagnostics were used in this study: microscale Raman spectroscopy and microscale thermoreflectance. Both methods use a low-energy, nonperturbing probe laser beam, whose arbitrary wavelength can be selected for a diffraction-limited focus that meets the need for micron-scale spatial resolution. Raman is exploited most frequently, as this technique provides a simple and unambiguous measure of the absolute device temperature for most any MEMS semiconductor or insulator material under steady state operation. Temperatures are obtained from the spectral position and width of readily isolated peaks in the measured Raman spectra with a maximum uncertainty near ±10 K and a spatial resolution of about 1 micron. Application of the Raman technique is demonstrated for V-shaped and flexure-style polycrystalline silicon electrothermal actuators, and for a GaN high-electron-mobility transistor. The potential of the Raman technique for simultaneous measurement of temperature and in-plane stress in silicon MEMS is also demonstrated and future Raman-variant diagnostics for ultra spatio-temporal resolution probing are discussed. Microscale thermoreflectance has been developed as a complement for the primary Raman diagnostic. Thermoreflectance exploits the small-but-measurable temperature dependence of surface optical reflectivity for diagnostic purposes. The temperature-dependent reflectance behavior of bulk silicon, SUMMiT-V polycrystalline silicon films and metal surfaces is presented. The results for bulk silicon are applied to silicon-on-insulator (SOI) fabricated actuators, where measured temperatures with a maximum uncertainty near ±9 K, and 0.75-micron in-plane spatial resolution, are achieved for the reflectance-based measurements. Reflectance-based temperatures are found to be in good agreement with Raman-measured temperatures from the same device.

ACKNOWLEDGEMENTS

TABLE OF CONTENTS

LIST OF FIGURES

LIST OF TABLES

1. INTRODUCTION

Microelectromechanical systems (MEMS) components are playing increasingly critical roles in Sandia-engineered systems and within the larger engineering community. MEMS components that have recently undergone evaluation for Sandia applications include: optical switching technologies, such as the discriminating micro-switch (DMS) [1, 2], vertical-cavity surface-emitting lasers (VCSELs) [3], thermal actuators for nonvolatile memory [4], and other microscale technologies such as the μChemLab [5]. The small thermal mass and high relative surface area of MEMS structures renders the thermal response of these systems critical. Meanwhile, the ever-shrinking length scales of these devices have revealed different thermophysical behavior from the macroscale, which is often poorly understood. Characterization of the thermophysics of MEMS structures requires, first and foremost, an accurate knowledge of the device temperature field and its gradients. Historically, Sandia has not possessed the capability for nonperturbing temperature diagnostics with the micron-scale spatial resolution required for experiments on working MEMS devices. The purpose of this LDRD project has been to meet Sandia's need for microscale thermal measurements through the development and application of two laser-based diagnostics for MEMS thermometry: microscale Raman spectroscopy and thermoreflectance.

The temperature diagnostics were selected based on a list of requirements for thermal MEMS measurements which included the following.

1. Spatial resolution on the order of 1 μm or better
2. Multi-point scanning measurements for 1-D or even 2-D profiling
3. Ability to probe "as-fabricated" MEMS without changes to device design
4. Little or no impact upon MEMS device function

Contact methods such as intrinsic RTDs or thermocouples and scanning thermal microscopy (SThM) [6] may impede device function or, in some cases, damage the device. Intrinsic temperature sensors will not meet the need for multi-point profile mapping, and may require more complex component designs as well as special fabrication runs, so that "as-fabricated" devices cannot be studied. SThM satisfies the profiling and resolution requirements, but is extremely expensive and requires modeling of the complex heat transfer between the probe tip and MEMS surface, which is often not well understood [6].

Optical methods are much more amenable to the requirements outlined above. Candidate optical methods for MEMS component thermometry include: infrared imaging [7], Raman spectroscopy [8, 9], surface thermoreflectance [10], and fluorescence imaging [11].

Fluorescence-based measurements often require that dopants or surface coatings be added to the sample [11], which add an additional and potentially complex step to the experiments and makes testing of "as-fabricated" MEMS difficult. Fluorescence doping can also require expensive design modifications, and may potentially change the thermophysical response of the microdevice.

Infrared (IR) imaging is the simplest optical thermometer, and provides insightful 2-D mapping data, which alone warrants its serious consideration. IR imaging requires no external optical excitation, as the thermal radiation emitted from the sample is simply imaged onto an IR-array detector using an infrared objective. The chief drawbacks of IR methods are the poor spatial resolution of far-field infrared imaging [4, 7] and systematic errors resulting from incomplete knowledge of the local device emissivity. IR imaging is also difficult on metal surfaces, where the emissivity is low, and on many semiconductors, which are at least partially transparent to infrared radiation.

Microscale Raman spectroscopy and thermoreflectance have been chosen for diagnostic development because they best meet all four criteria listed above. Both methods employ probe laser beams of arbitrary wavelength, and visible laser frequencies are selected to achieve near-diffraction-limited probe-laser spots with micron-scale spatial resolution. The probe-laser spots can readily be scanned to provide 1-D and/or 2-D mapping of MEMS surfaces under steady state operation. Raman and reflectance signatures are sufficiently strong, such that very low levels of non-perturbing laser power can be employed in the measurements with no change to device function. Both methods merely require optical access to the MEMS surface so that "as-fabricated" devices are readily tested.

With Raman spectroscopy, a probe laser beam of arbitrary wavelength is coupled to an optical microscope and focused to a micron-sized spot on the device surface. The probe-laser photons couple to optical phonons in the material to scatter light at frequencies that are spectrally shifted from the probe-laser line by the allowed phonon energies. The phonon energies, phonon lifetimes and relative phonon populations are all strong functions of temperature, and result in changes in the peak positions, peak widths and relative peak heights in Raman spectra, which are exploited for diagnostic purposes. The fundamental building block of MEMS at Sandia is polycrystalline silicon, or "polysilicon" and Raman has been extensively used for probing of mechanical stress in such solid-state materials [12-14]. Fundamental investigations of the temperature-dependent properties of bulk-silicon Raman spectra were first conducted in the 1970s and 1980s [15-17] and provide a foundation for Raman temperature diagnostics. Since

then, some applications of microscale Raman thermometry to microelectronics [8, 9] and MEMS [18, 19] began to appear in the 1990s and 2000s.

We have pursued thermoreflectance as a complement to Raman. The reflectance diagnostic exploits small-but-detectable changes in the temperature-dependent surface reflectivity to a probe laser beam. The sensitivity of this change with temperature is determined by the thermoreflectance coefficient, κ, which relates the change in reflectivity per unit change in temperature. Typically, κ is on the order of 10^{-4}–10^{-6} K^{-1} and depends on the wavelength that is used to probe the surface [20-23]. In addition to being a purely optical, non-invasive technique, thermoreflectance has the potential for providing micron-scale spatial resolution and sub-nanosecond temporal resolution [6, 24-27]. While spatial resolution is limited by the diffraction limit of the optics involved in the detection scheme, the theoretical limit of the temporal resolution is determined by the order of the processes involved in the reflectance, which can be on the order of picoseconds in metals [20]. The drawbacks to this technique are the challenging calibration of the thermoreflectance coefficient and potentially altered reflectance calibrations with deflection/deformation of the surface during the measurement.

In this report, we document the results of the Raman and thermoreflectance diagnostic-development and application efforts. We begin with a brief discussion of the physics of spontaneous Raman scattering, which is followed by a description of our Raman optical system, and the temperature-dependent characteristics of the Raman spectra of silicon; the chief building block of MEMS devices. We then present the results of several applications of Raman for spatially resolved steady-state temperature mapping on real MEMS devices, including silicon-fabricated MEMS and GaN-fabricated transistors, which illustrates the applicability of Raman to a wide class of materials. The potential of Raman for simultaneous mapping of temperature and mechanical stress is also presented to illustrate the utility of Raman as a multi-parameter diagnostic. Results from the thermoreflectance diagnostic-development effort are discussed, including calibration of the reflectance technique on bulk and polycrystalline silicon and metal surfaces. Thermoreflectance thermometry is applied to a working electro-thermal actuator and a comparison of thermoreflectance-based temperatures versus a Raman standard reveals good agreement between the two techniques. The report concludes with a description of several Raman-variant techniques for improved spatial and temporal resolution, which form the basis for continued near-term diagnostic-development efforts.

2. RAMAN SCATTERING TECHNICAL BACKGROUND

2.1 Optical Processes: Electric-Dipole Radiation

Raman is an inelastic light-scattering process in which a small fraction of the incident photons from an arbitrary light source are scattered with a spectral frequency (energy) shift that is characteristic of the scattering medium. Linear light-scattering processes are described in Fig. 1a, where a linearly polarized laser light source with electric field, **E,** induces an oscillating dipole moment, or *polarization*, upon the electron charge field in the scattering medium. The radiating dipole emits in the characteristic toroidal pattern [28], with zero emission along the dipole axis and radiation maxima at normal angles to the dipole. For linear light-scattering processes, the total light scattering is proportional to the strength of the induced dipole moment and the incident laser field,

$$\mathbf{E}_s \sim \mathbf{P} = \varepsilon_o \, \underline{\underline{\alpha}} \, \mathbf{E}_l \quad , \tag{1}$$

where $\sim$ indicates proportionality, ε_o is the free-space permittivity, $\mathbf{E}_s$ is the scattered electric field, $\mathbf{P}$ is the induced polarization, $\mathbf{E}_l$ is the incident laser field and $\underline{\underline{\alpha}}$ is termed the electric polarizability, which quantifies how readily the scattering medium is polarized by the incident laser field.

In general, the electric fields and induced polarization are vector quantities so that $\underline{\underline{\alpha}}$ is a rank-2 tensor, from which we drop the vector-tensor notation for convenience. The polarizability is generally expanded in terms of the equilibrium and displaced positions of the medium's atomic structure,

$$\alpha = \alpha_o + \left(\frac{\partial \alpha}{\partial Q} \right) \delta Q \quad , \tag{2}$$

where Q is a time-varying internuclear displacement and α_o and $\partial \alpha / \partial Q$ are the equilibrium polarizability and time-varying polarizability derivative, respectively. If the incident laser field is at frequency, ω, and the internuclear separation is oscillating at some natural frequency, Ω, then $E_l \sim E_{l,o} \cos \omega t$ and $\delta Q \sim \delta Q_o \cos \Omega t$ such that the scattered electric field is now written as,

$$E_s \sim \alpha_o E_{l,o} \cos \omega t + \left(\frac{\partial \alpha}{\partial Q} \right) E_{l,o} \cos \omega t \cos \Omega t \quad , \tag{3}$$

A.C. Eckbreth, "Laser Diagnostics for Combustion Temperature and Species," 2nd Ed, Gordan and Breach, 1996.
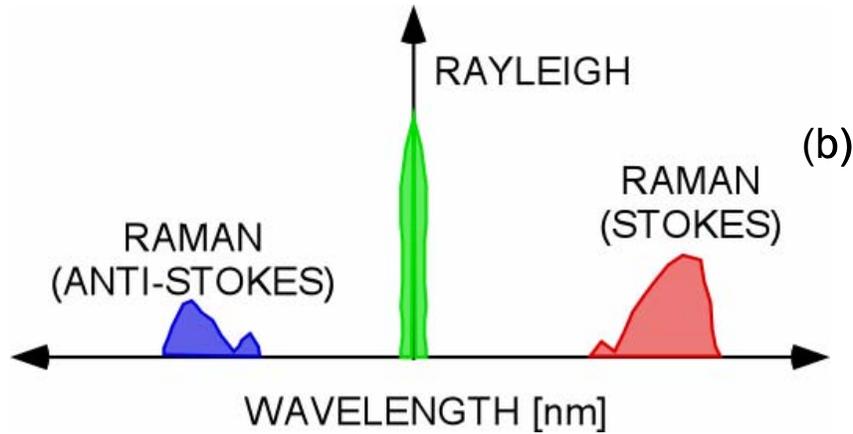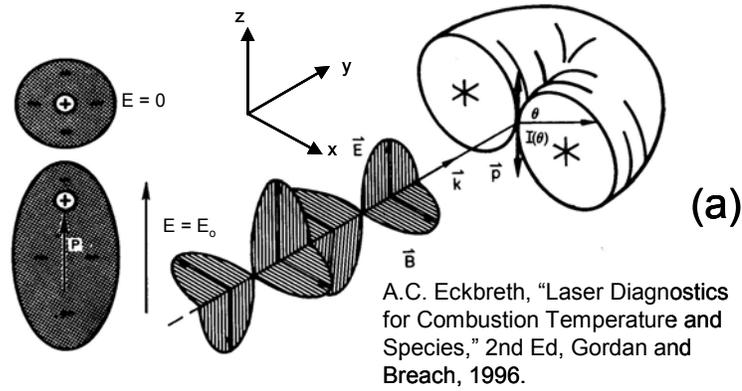
Figure 1 – Electric-dipole light-scattering principles: a dipole induced by a linearly polarized laser field is shown in part (a) [28] while linear light-scattering spectra are depicted in (b).

which may be rewritten in this manner following application of a simple trigonometric identity,

$$E_s \sim \alpha_o \, E_{l,o} \cos \omega t + \left(\frac{\partial \alpha}{\partial Q} \right) E_{l,o} \left[\cos (\omega + \Omega) t + \cos (\omega - \Omega) t \right] \quad . \tag{4}$$

As depicted in Fig. 1b, the first term in Eq. 4 is the elastic, or Rayleigh, scattering contribution, which represents dipole scattering at the incident laser frequency, ω[†]. The Rayleigh peak is by far the strongest of the linear scattering processes. The second term represents the inelastic, or vibrational Raman components, which are spectrally shifted to the Stokes $(\omega - \Omega)$ and anti-Stokes $(\omega + \Omega)$ sides of the probe laser by characteristic vibrational resonances of the scattering medium. In this manner, Raman is species selective since different compounds display distinct molecular resonance frequencies that are readily identifiable in Raman spectra.

[†] Rotational Raman scattering in fluids, which occurs very close to the probe-laser line, is also accounted for in this term.

2.2 Impact of Solid-State Physics on Raman Spectra

In solid-state materials, Raman scattering arises through the interaction of probe laser light with quantized lattice vibrations, or *phonons* [29, 30], such that Ω in Eq. 4 now represents the optically coupled phonon-mode frequency. Raman selection rules describe the change in frequency, ω (energy), and wave vector, $\mathbf{k}$ (momentum), for the inelastic scattering process [30],

$$\omega_R = \omega \pm \Omega \quad , \tag{5a}$$

$$\mathbf{k}_R = \mathbf{k} \pm \mathbf{K} \quad , \tag{5b}$$

where ω_R and $\mathbf{k}_R$ refer to Raman-scattered photons, ω and $\mathbf{k}$ refer to the probe-laser beam, and Ω and $\mathbf{K}$ refer to the phonon. In the Stokes process, $\omega_R = \omega - \Omega$, and a red-shifted Raman photon results from the creation of an optical phonon at Ω with a loss of optical energy. The anti-Stokes process, $\omega_R = \omega + \Omega$, creates a blue-shifted Raman photon from the annihilation of a thermally generated optical phonon and a gain of optical energy.

We consider the Raman spectra of silicon as an example because Si is such a ubiquitous material in MEMS fabrication. Sample Raman spectra from the P4 layer of a SUMMiT-V-fabricated (Sandia Ultraplanar Multi-level MEMS Technology [31], see section 5.2.2 for further description) polysilicon part are provided in Fig. 2. The spectra have been recorded for several different temperatures with the sample placed in an optically accessible and temperature-controlled hot stage. The Raman spectra of polysilicon are quite simple, displaying single isolated peaks on the Stokes and anti-Stokes side, which arise from the triply degenerate optical phonon modes of the material. As temperature increases, the location of the Raman peaks shifts toward lower energies, the width of the Raman peaks becomes greater, and the relative strength of the anti-Stokes peak is increased. All of these phenomena can be exploited for temperature diagnostics and a rudimentary description of the physics of each of these temperature-dependent processes is provided in the following subsections.

2.2.1 Raman Peak Position: Phonon Frequency

Phonon vibrational modes and their dispersion can be modeled as classical spring-mass oscillator systems if the laws (spring constants) for the interatomic forces within the solid-state lattice are known. Kittel [30] suggests the following form in the nearest-neighbor approximation for an example system with two atoms per symmetric primitive basis cell,
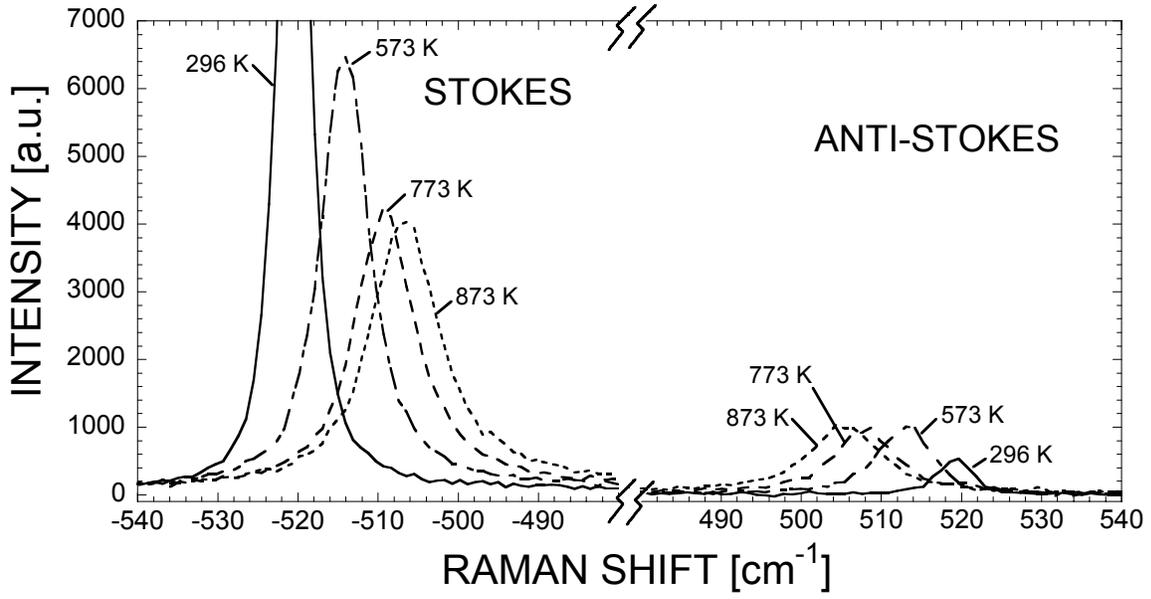
Figure 2 – Raman spectra obtained from a SUMMiT-V P4 polysilicon film. The spectra result from the triply degenerate optical phonon in Si. The horizontal axis represents the shift in wavenumbers from the probe laser line. Note the broken axis for Raman shifts between +480 and -480 cm^{-1}.

$$M_u \frac{d^2 U_s}{dt^2} = C(V_s + V_{s-1} - 2U_s) \quad , \tag{6a}$$

$$M_v \frac{d^2 V_s}{dt^2} = C(U_{s+1} + U_s - 2V_s) \quad . \tag{6b}$$

In Eqs. 6 U_s and V_s are the displacements of atomic species u and v in plane s, M_u and M_v are the atomic masses of u and v, and C is a proportionality factor in the form of a simple Hooke-type force between neighboring atoms. Eqs. 6 admit traveling wave solutions in terms of the spacing between identical lattice planes, a, the phonon temporal frequency, Ω, and phonon wave vector, **K**, such that $|\mathbf{K}| = K = 2\pi/\lambda$, where λ is the length of the phonon elastic wave.

$$U = U_o \exp(isKa)\exp(-i\Omega t) \tag{7a}$$

$$V = V_o \exp(isKa)\exp(-i\Omega t) \tag{7b}$$

Upon substitution of Eqs. 7 into Eqs. 6, we obtain a homogeneous-linear system for the amplitudes U_o and V_o, which can be solved to obtain a dispersion relation between Ω and K. A plot of the dispersion relation is provided in Fig. 3. Raman photon-phonon interactions occur through the optical phonon branch at the center of the Brillouin zone where $K \rightarrow 0$ [15, 16]. These coherent, long-range phonons typically decay to multiple acoustic phonons after some
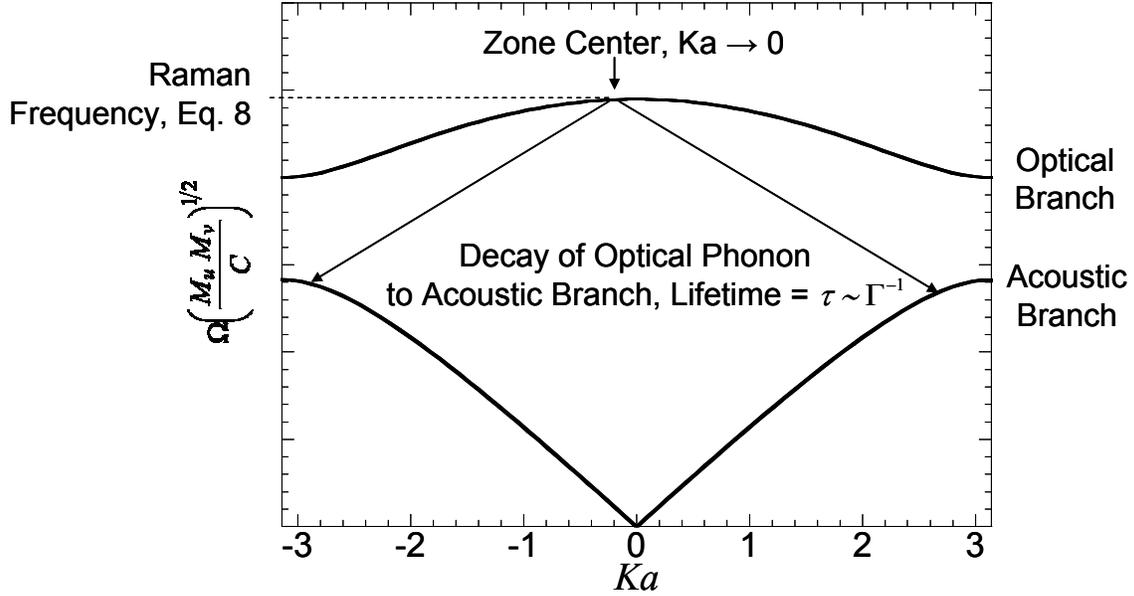
Figure 3 – Phonon frequency-wavenumber dispersion relation obtained from the solution of Eqs. 6. The solution for the full Brillouin zone is shown. The phonon vibration frequency, Ω, is plotted against the magnitude of the phonon wave vector, K, multiplied by the spacing between identical lattice planes, a. Both the optically and acoustically coupled branches are shown. The Raman process couples to long-range optical phonons near the zone center at $Ka = 0$. The Raman peak position is dictated by the zone-center frequency, while the Raman peak width, Γ, is inversely proportional to the life time of the zone-center optical phonon as it decays to the acoustic branch.

temperature-dependent lifetime, τ. We examine the optical-branch dispersion for the case of small K to illustrate the dependence of the Raman frequency on the forces within the lattice [30].

$$\Omega^2 = 2C\left(\frac{1}{M_u} + \frac{1}{M_v}\right) = \frac{2}{M_r} \quad (K \to 0) \quad . \tag{8}$$

This solution is independent of the small value of K and shows that the frequency of the zone-center optical phonons coupled to the Raman process can be expressed in terms of a Hooke-type force factor and the system reduced mass, M_r. This is generally true even for more realistic systems than the example of Eqs 6.

For the case of $C = constant$, the system behaves as a harmonic oscillator at constant frequency. However, solid-state systems with realistic interatomic potentials display nonlinear forces, such that C is not constant and the phonon energy changes with temperature and strain. As explained in an excellent review article by Lucazeau [14], temperature-dependent shifts in Ω arise from two contributions to the force nonlinearity: (1) a volumetric expansion and (2) a

constant-volume effect. In the first case, thermal and/or mechanical strain combines with realistic interatomic potentials, such that C now depends on the displacements of atoms, and Ω changes with the lattice spacing. In the latter case, temperature-dependent changes in lattice vibrational energy through the Bose-Einstein statistics alter the interatomic forces. Since the force constants, C, are altered by both thermally and mechanically induced lattice strain, the Raman peak position is influenced by both temperature and mechanical stress. This leads to potential bias errors in peak-shift-based Raman thermometry in applications with significant stress applied to the MEMS device.

2.2.2 Raman Peak Width: Phonon Lifetime

The width of the Raman peaks in Fig. 2 is determined principally from the lifetime of the optical phonons coupled to the Raman process. Heisenberg's energy-time uncertainty [32] describes the relationship between uncertainty in the phonon energy and the time span for which the phonon is observed,

$$\Delta E = \hbar \Delta \Omega \sim \frac{\hbar}{\tau} \sim \Gamma \quad , \tag{9}$$

where ΔE is the uncertainty in the energy of a single phonon, $\Delta \Omega$ is the uncertainty in the phonon frequency, $\hbar$ is the Planck constant divided by 2π, τ is the lifetime of the phonon, and Γ is the measured full-width-at-half-maximum (FWHM) of the Raman line. If there is a large assembly of phonons coupled to the Raman process, each phonon contributing to the observed Raman line fluctuates through the frequency range $\Delta \Omega \sim 1/\tau$, with a resultant natural linewidth of Γ observed in the Raman spectrum.

As described in Fig. 3, the optical phonons coupled to the Raman process typically decay to the acoustic branches via phonon-phonon or phonon-boundary scattering. In general, as temperature increases, the number of phonons available for phonon-phonon scattering increases, with a decrease in the lifetime of the long-range Raman-coupled phonons; all of which acts to decrease τ and increase Γ. The Raman linewidth is primarily dependent upon temperature and no stress-induced bias should be observed in linewidth-based Raman thermometry. In polycrystalline materials with significant phonon-boundary scattering, the phonon lifetime is further influenced by the grain size with an increase in Raman linewidth. Care should be taken to calibrate the Raman linewidth on the same polycrystalline materials used in the MEMS application, and to ensure that the device under test has been well-annealed, so that any redistribution of the grain structure at high-temperature does not bias the measurement.

2.2.3 Anti-Stokes to Stokes Ratio: Phonon Thermal Occupation

The ratio of anti-Stokes to Stokes intensities is a third piece of temperature-dependent information to be extracted from solid-state Raman spectra. As a result of photon-phonon energy exchange during the Raman process, Stokes (red-shifted) processes arise from the creation of a phonon, while anti-Stokes (blue-shifted) processes result from phonon annihilation. Hart *et al.* [15], explain that the intensities of the Stokes and anti-Stokes Raman lines are related to the average thermal energy of the optically coupled phonon modes by,

$$I(\omega - \Omega_\mathbf{k}) \sim n_\mathbf{k} + 1 \quad \text{(Stokes line)} \quad, \tag{10a}$$

$$I(\omega + \Omega_\mathbf{k}) \sim n_\mathbf{k} \quad \text{(anti-Stokes line)} \quad, \tag{10b}$$

where I is the Raman-scattered intensity, and $n_\mathbf{k}$ is the average quantum number representing the thermal vibrational energy, $(n_\mathbf{k} + 1/2)\hbar\Omega_\mathbf{k}$, within the optically coupled phonon mode at wave vector **K**, as given by the Bose-Einstein distribution,

$$n_\mathbf{k} = \frac{1}{\exp(\hbar\Omega_\mathbf{k}/kT) - 1} \quad . \tag{11}$$

The intensity ratio of the two lines is then given by,

$$\frac{I(\omega + \Omega_\mathbf{k})}{I(\omega - \Omega_\mathbf{k})} = \frac{n_\mathbf{k}}{n_\mathbf{k} + 1} = \exp(-\hbar\Omega_\mathbf{k}/kT) \quad, \tag{12}$$

where $\hbar$ is the reduced Planck constant, k the Boltzmann constant and T is the temperature. In Eq. 12, we can see that as temperature decreases the relative intensity of the anti-Stokes peak vanishes, as there are a negligible number of thermally generated optical phonons available for annihilation in the anti-Stokes process. As temperature increases, the anti-Stokes intensity grows, but the sensitivity of the intensity ratio decays as the phonon thermal population becomes fully excited. The Stokes-to-anti-Stokes ratio is solely dependent on temperature, but the method loses sensitivity at high temperatures and is experimentally less convenient as it requires long acquisition times to obtain sufficient anti-Stokes signal.

3. RAMAN OPTICAL SYSTEM

The experiments were conducted using a Renishaw (Gloucestershire, UK) "inVia" integrated Raman microscope, which is shown in Fig. 4. The instrument utilizes the 488-nm line of a continuous-wave Ar$^+$ laser as the Raman probe source. Laser power delivered to the sample can be varied by several orders of magnitude by adjusting the current to the laser tube and placing neutral-density filters in the beam path. The probe laser is focused onto the sample under test by a 100× objective of 0.75 numerical aperture. The 1/e penetration depth of the 488-nm wavelength laser beam in silicon was estimated at 0.635 μm. The Raman signal is collected in backscatter through the microscope objective, dispersed by a grating spectrograph and detected using a frontside-illuminated, deep-depletion, thermoelectrically cooled CCD camera, with a dispersion of the Raman signal at the CCD of 0.95 cm^{-1}/pixel. The bandpass (resolution) of the spectrograph is 2.8 cm^{-1} for the 65-μm-wide entrance slits used to maximize the detected Raman signal at the expense of some spectral resolution.

Beam powers supplied to silicon and polysilicon MEMS devices were typically limited to 50 μW (4.4 kW/cm^2 spatially averaged flux for a 1.2-μm-diameter Raman probe size) to minimize laser-induced heating of the samples. Minimal sample heating was confirmed by reducing the probe-laser power until no change in the Si peak position of Raman spectra acquired from room-temperature polysilicon MEMS thermal actuators was observed. Scaling arguments[*] were utilized to estimate a temperature rise of ~ 0.7 K for an absorbed flux of 50 μW delivered in a 1.2-μm-diameter spot and fully absorbed at a polysilicon surface.

An image of the probe-laser spot on a polysilicon thermal actuator beam is provided in Fig. 5a. The laser spot is seen to be less than the 3-μm width of the beam, and it is clear that our Raman probe is capable of resolving this small-scale device feature. The size of the laser spot delivered by the optical system was first measured by translating a razor blade through the beam's focus and metering the total power transmitted past the knife edge as it blocked the focused beam. These data are shown in Fig. 5b, where the transmitted laser power is plotted against the knife-edge position and we see that the 10% and 90% transmission points are separated by ~ 0.4 μm.

---

[*] Consider an energy transfer of q = 50 μW that is delivered in a spot size of diameter δ = 1.2 μm to polysilicon with a conductivity of k = 60 W/m-K at a representative temperature of T = 250 $^{\circ}$C. The length of the laser-induced temperature perturbation will scale with δ so that the laser-induced heat flux scales as $q'' \sim q/\delta^2 \sim k\,\Delta T/\delta$. Solving for the laser-induced temperature rise we find that $\Delta T \sim 0.7$ K, which is much less than the observed temperature changes in thermal MEMS devices and less than the ±10-11 K uncertainty in the peak-position-based Raman temperatures. This estimate is conservative as it is based on one-dimensional conduction and because it assumes all of the laser energy is absorbed at the surface of the polysilicon layer.
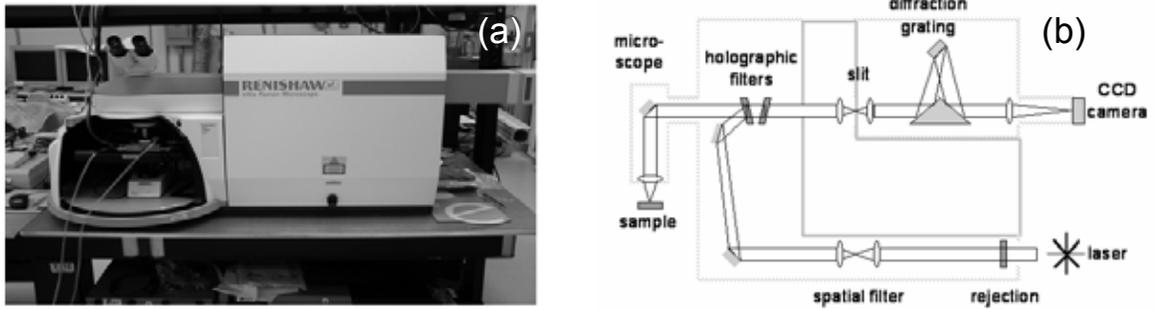
Figure 4 – Integrated Raman microscope fabricated by Rensihaw and shown as installed (a). Optical schematic of Raman microscope (b).
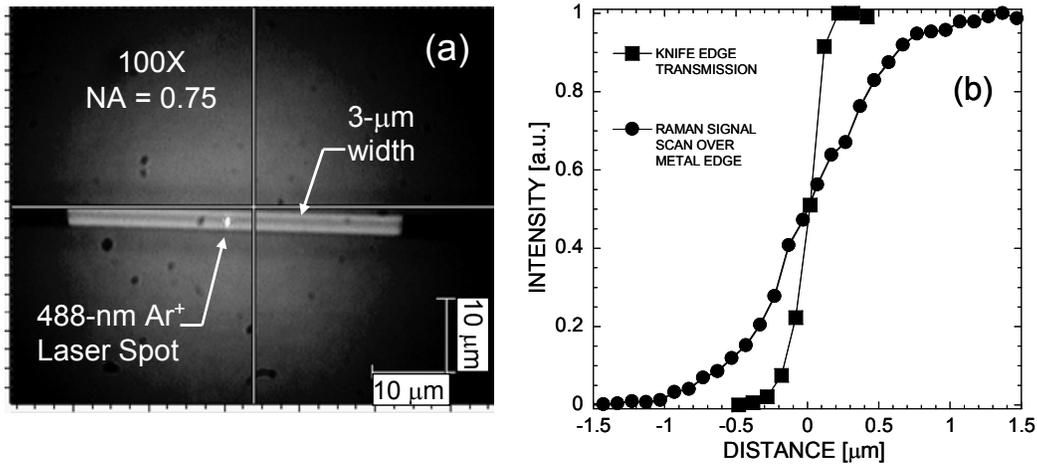
Figure 5 – Illustration of the in-plane spatial resolution afforded by the Raman technique: (a) digital photograph of 3-μm wide P34 thermal actuator, observed with a 100× magnification objective of 0.75 numerical aperture, and showing an image of the 488-nm-wavelength probe-laser spot, (b) measurements of the probe-laser spot size via knife-edge transmission in air and by metering the integrated Raman signal as the laser-spot is scanned over a Si-to-Al transition.

The in-plane resolution of the Raman data was better quantified by scanning the laser spot over a polysilicon sample onto which aluminum lines had been deposited. No detectable Raman signal was observed from Al, and images of the Al-to-Si transition at 100× magnification revealed that this transition took place in a span of less than 0.1 μm. The laser spot was scanned across the edge of the metal line in 0.1-μm increments and the spectrally integrated Raman signal was plotted against the laser-spot position, as also shown in Fig. 5b. If we define an in-plane resolution based on 10% and 90% of the maximum Raman intensity, we arrive at an estimate of 1.2 μm. This value is three times larger than the measured spot size in air. This difference between knife-edge and signal integration approaches for estimation of the in-plane resolution bas been previously observed Gardiner et al. [33] who attribute the difference to spreading of the laser probe inside their silicon film.

4. TEMPERATURE CALIBRATION FROM SILICON RAMAN SPECTRA

Raman spectra were obtained from both single-crystal and polycrystalline silicon samples, which were placed in a temperature-controlled and optically accessible stage. Peak positions, full-width-at-half-maximum (FWHM) peak widths, and spectrally integrated Stokes and anti-Stokes intensities were determined from fits of a Voight lineshape function to each isolated Raman line,

$$V(\Omega) = A_l \frac{(\Gamma_l/2)^2}{(\Gamma_l/2)^2 + (\Omega - \Omega_o)^2} + A_G \exp\left(-2.773 \frac{(\Omega - \Omega_o)^2}{\Gamma_G^2}\right) \quad . \tag{13}$$

The Voight function captures both the natural Lorentzian Raman lineshape as well as the impact of a Gaussian instrument function associated with finite spectral resolution. In Eq. 13, A_l and A_G are the amplitudes of the Lorentzian and Gaussian portions, respectively, Γ_l and Γ_G are the respective Lorentzian and Gaussian full-width at half maximum (FWHM) linewidths, and Ω_o is the line-center frequency, set equal for both components of the lineshape. Fitting of the spectra to the expected Voight functional form allows for determination of the peak position with a precision of $\pm 1/16$ pixel (0.055 cm^{-1}) at room temperature and $\pm 1/9$ pixel (0.095 cm^{-1}) at 700 K, as determined from fits to large ensembles of Raman spectra. Composite linewidth data were extracted by numerically locating the roots of the half-maximum points of the Voight profile. A typical Voight fit result is shown in Fig. 6. It should be noted that the measured linewidth values are slightly broadened by the finite spectral resolution our instrument so that natural Raman linewidths are not measured using this approach. This in no way impacts the diagnostic utility of the measured linewidth data.

A plot of the measured temperature dependence of the Stokes-shifted Raman peak position is presented in Fig. 7. A linear dependence is observed over the calibrated 300 to 970 K temperature range for both single-crystal Si and polycrystalline P3 and P4 SUMMiT-V layers, with a slope of $d\Omega/dT = 0.024 \pm 0.00016$ cm^{-1}/K for all layers tested. A distinct offset of 0.5 cm^{-1} is observed between the single-crystal and polycrystalline Si data, which may be a result of residual stress in the polysilicon films. This offset in the absolute peak position results in a temperature bias of 21 K if it is not considered in data processing.

The temperature dependence of the linewidth (FWHM) of the Stokes-shifted Raman peaks is plotted in Fig. 8. The linewidth data are clearly delineated between single-crystal silicon, SUMMiT-V-fabricated P3 films deposited on 600-nm-thick thermal oxide layer, and SUMMiT-

V-made P34 MEMS components. The results for single-crystal Si exhibit the lowest Γ values, as would be expected from Eq. 9, since these specimens had the greatest degree of long-range order and hence the longest phonon lifetimes. The polysilicon samples exhibit larger peak widths as a result of finite grain size and decreased optical phonon lifetime resulting from grain-boundary phonon scattering. Raman signatures from the P34 and P3 specimens originate from the upper P4 and P3 layers, respectively. These SUMMiT-V layers are deposited in an essentially identical manner and we would expect their average grain size to be similar. Nevertheless, the linewidth data clearly suggest a greater degree of long-range order for the P3 films.

A plot of the ratio of anti-Stokes to Stokes integrated-band intensities is provided in Fig. 9. The data are plotted alongside an exponential fit of form $I_{AS}/I_S = A\exp(-B/T)$, which is suggested by the analytically derived functional form given in Eq. 12. We observe the expected exponential increase of the ratio, as the number of thermally generated phonons available for annihilation in the anti-Stokes process increases with temperature. However, this integrated-band-ratio metric was not used for diagnostic purposes because it required long acquisition times to detect sufficient anti-Stokes signal, and because the sensitivity of the method decreases at high temperatures.

The temperature-dependent properties of Raman peak position and linewidth, shown in Figs. 7 and 8, were used as metrics for thermal diagnostics. Stokes-shifted Raman peak position was found to be the most precise and robust indicator, and this metric was used for all of the Raman thermometry results presented here, with the exception of applications where significant mechanical strain was present in the sample. Stokes-shift-based temperatures were determined from the Stokes peak position using,

$$T = T_o + \left(\frac{\partial \Omega}{\partial T}\right)^{-1} (\Omega - \Omega_o) \quad , \tag{14a}$$

which, for silicon-based MEMS takes the form,

$$T = T_o + \frac{\Omega_o - \Omega}{0.024 \ \mathrm{cm}^{-1}/\mathrm{K}} . \tag{14b}$$

In Eqs. 14, Ω_o is the measured Stokes-shifted peak position at the ambient temperature, T_o, and Ω is the peak position at the device temperature, T.

As discussed in Section 2.2.1, mechanical strain impacts the interatomic lattice forces in a similar manner to lattice thermal expansion, and significant bias errors in peak-based

temperatures can occur when stress is applied to a sample (see Sections 6 and 7 below). In cases where mechanical strain was an issue, the measured linewidth was used as a temperature metric. To first order, the measured linewidth data are dependent on temperature through thermal changes to the phonon lifetime and are independent of strain, with some sample-based dependence due to grain size. Relative to a peak-based temperature metric, linewidth-based temperatures are less precise as a result of increased scatter in a typical Voight-linewidth determination. The linewidth-temperature data shown in Fig. 8 are well-represented by the linearized quadratic-polynomial fits shown in the plot,

$$\Gamma = A(T + B)^2 + C \ ,$$ (15a)

such that linewidth-based temperatures were computed from the following form, when noted in this manuscript.

$$T = \sqrt{\frac{\Gamma - C}{A}} - B$$ (15b)
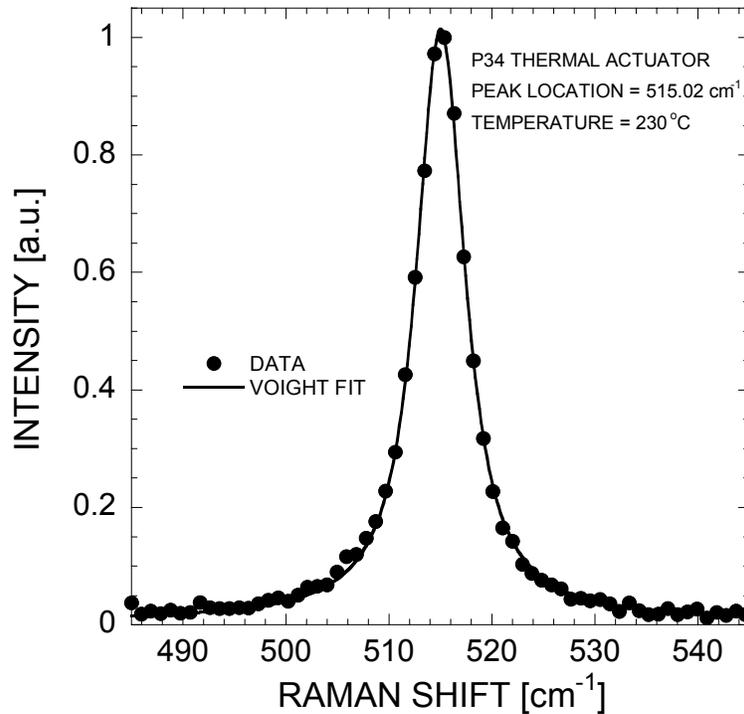
Figure 6 – Representative Voight curve-fit results for an isolated Raman peak obtained from a polysilicon thermal actuator.
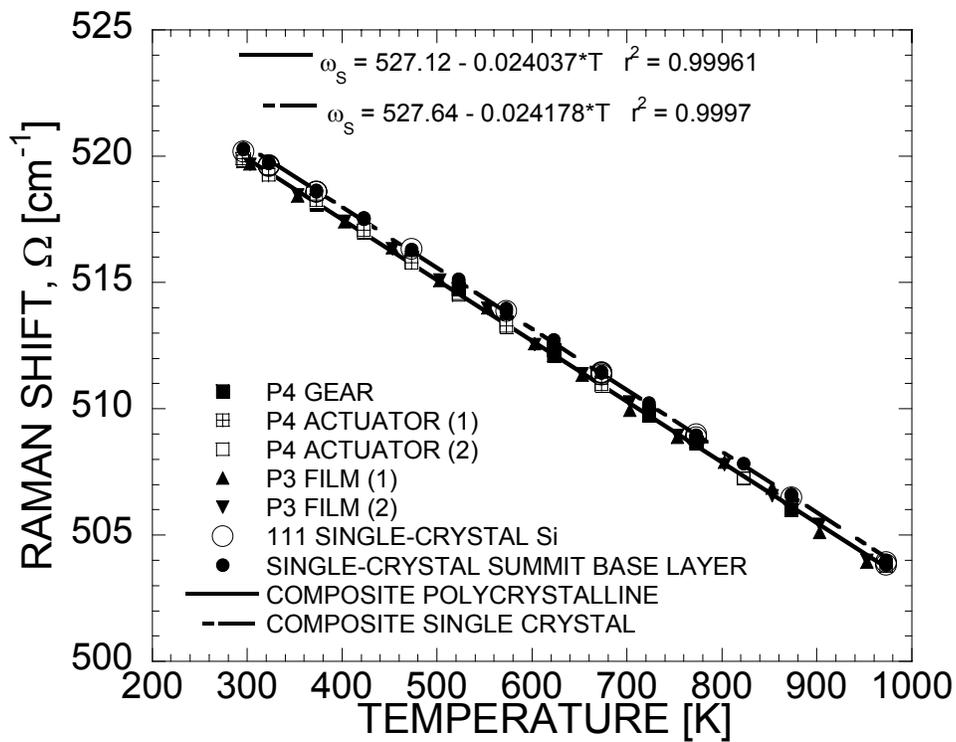
Figure 7 – Temperature dependence of the measured Stokes-shifted Raman peak position for bulk-silicon samples and SUMMiT-V-fabricated polysilicon films. The measured values are indicated by symbols, while line elements represent linear fits to the data.
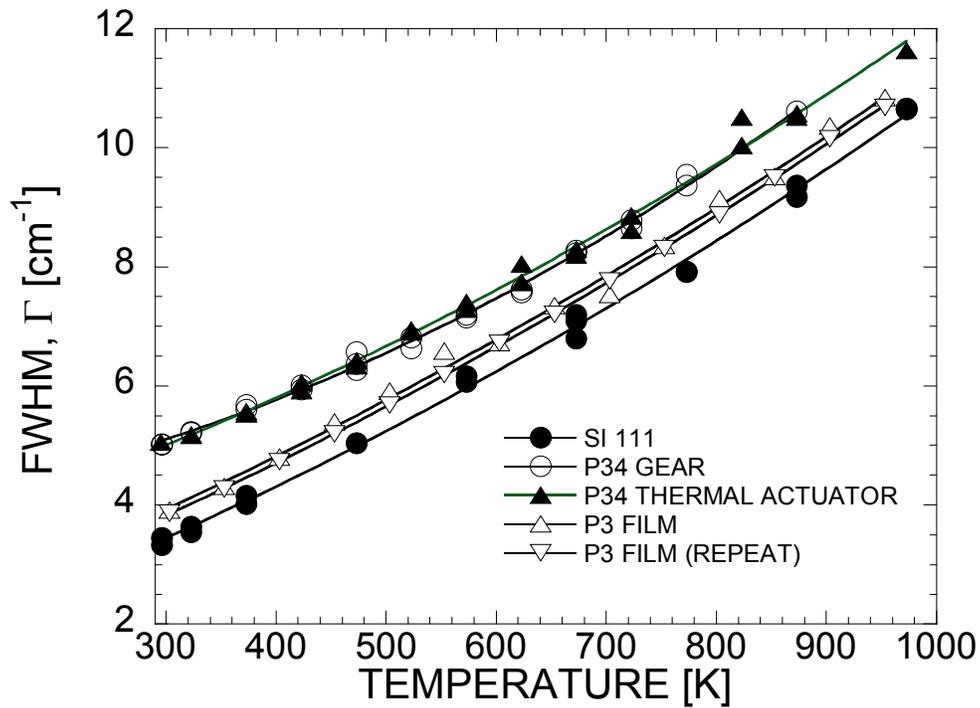
Figure 8 – Temperature dependence of the measured full-width-at-half-maximum (FWHM) linewidth values for several bulk-silicon samples and SUMMiT-V-fabricated polysilicon films. The data are indicated by symbols, while the solid lines represent quadratic fits.
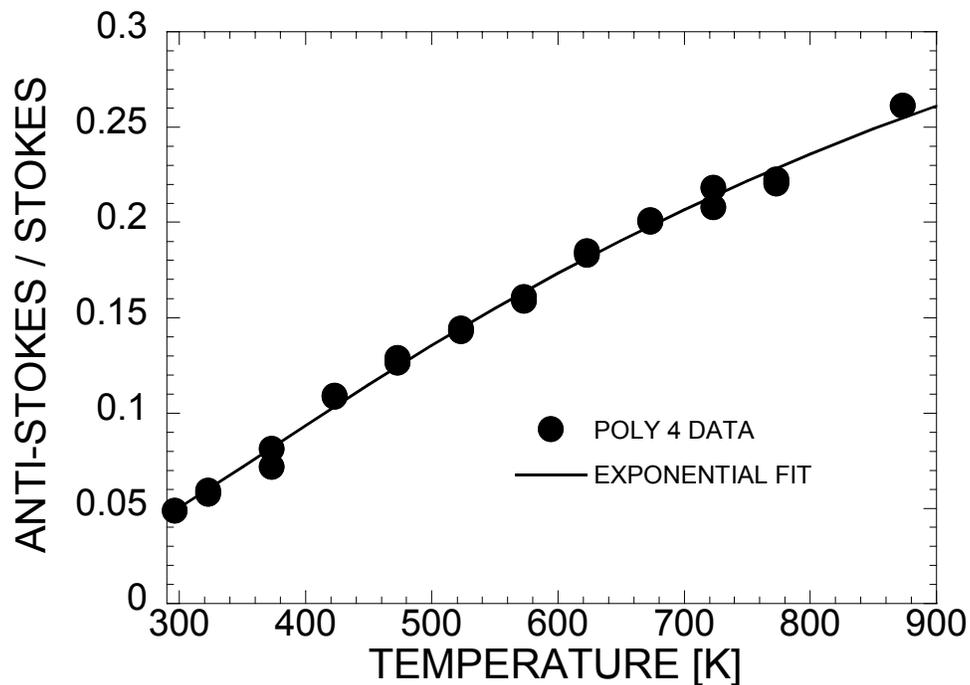
Figure 9 – Temperature dependence of the anti-Stokes to Stokes intensity ratio for a SUMMiT-V-fabricated poly-4 film.

5. APPLICATIONS OF RAMAN SPECTROSCOPY TO MEMS DEVICE THERMOMETRY

5.1 SUMMiT-V- Fabricated V-Shaped Thermal Actuators

5.1.1 Background

Surface micromachined electro-thermal actuators have seen a surge in interest for active MEMS applications ranging from adaptive optics to nonvolatile memory and mechanical systems [34]. Vis-à-vis more conventional electro-static actuation of MEMS, electro-thermal (ET) actuators provide superior force-displacement characteristics while operating at much lower voltages, which are compatible with commercial microelectronics and CMOS technologies. The convenience of fabrication of ET actuators by surface micromachining of polycrystalline silicon (polysilicon) facilitates versatile actuator design that can be optimized to a particular application in a cost-effective manner. This desire for optimal actuator design has been the impetus for development of several thermal and thermo-mechanical models of microscale ET actuator performance [4, 35-39]. Validation of these ET actuator models has been performed against integral measures of device performance, such as actuator displacement, force and dissipated power. These engineering metrics provide a useful measure of device functionality, but rigorous validation of any thermal model requires a detailed comparison of the predicted temperature field against high-quality experimental data. We report what we believe to be the first spatially resolved surface-temperature-profile measurements from working micron-scale ET actuators. The temperature data are intended for validation of analytical and computational models of actuator performance.

5.1.2 V-Shaped ET Actuator Design

A Scanning Electron Microscope (SEM) image of a SUMMiT-V-fabricated actuator design, typical of the devices under study, is shown in Fig. 10 [4]. This chevron design is characterized by one or more V-shaped legs which span a center shuttle. When electrical current is supplied to the device, the power dissipated in the electrically resistive actuator beams results in their thermal expansion and an amplified displacement of the center shuttle, which acts as a contact point for the active MEMS device driven by the actuator.

We have mapped the 1-D temperature profiles along a single actuator beam for five combinations of actuator design and applied current, as summarized in Table 1. Two different SUMMiT-V-made [31, 40, 41] actuator-beam cross sections were studied here: (1) a P34 design,
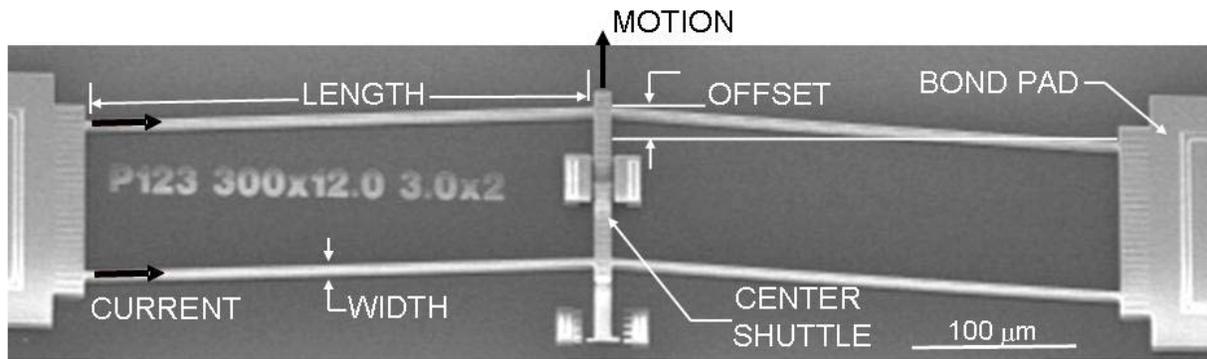
Figure 10 – Scanning Electron Micrograph (SEM) image of a V-shaped electro-thermal actuator, typical of the devices studied. Dimensions used to characterize the devices listed in Table 1 are defined in the figure.

where the lower P1 and P2 structural layers have been removed, and (2) a P123 design, where the upper P4 layer has been removed. The P34 design results in a larger separation between the actuator beams and the thermally massive device substrate. All actuator beams studied were 3 μm in width and 6.5-6.75 μm thick. All designs had 300-μm-long beams with 12-μm offset (Fig. 10) with the exception of experiment #1, where a P34 beam of 230-μm length and 4-μm offset was studied.

5.1.3 Temperature Profiles for V-Shaped ET Actuators

The Raman Stokes-shift method and Eqs. 14 were used to obtain the actuator device temperature profiles shown in Fig. 11. Temperature profiles were mapped along a single beam for the 5 experiments summarized in Table 1 by scanning the Raman probe-laser spot along the beam axis and integrating the spectra for 10-60 seconds, depending upon signal-to-noise ratio, which declines with increasing temperature. The temperature profiles are all qualitatively similar. A region of steep temperature gradient exists in the vicinity of the actuator bond pad,

Table 1 – Summary of V-shaped actuator geometries and applied current loadings for the Raman temperature-mapping experiments.

EXPT #	BEAM STRUCTURAL LAYERS	GAP TO SUBSTRATE [μm]	BEAM LENGTH [μm]	OFFSET [μm]	BEAM WIDTH [μm]	BEAM THICKNESS [μm]	APPLIED CURRENT [mA]	MEASURED VOLTAGE [V]
1	P34	6.5	230	4	3	6.5	11.25	4.70
2	P34	6.5	300	12	3	6.5	10.56	5.66
3	P34	6.5	300	12	3	6.5	8.89	4.21
4	P123	2	300	12	3	6.75	13.62	7.77
5	P123	2	300	12	3	6.75	11.43	5.50
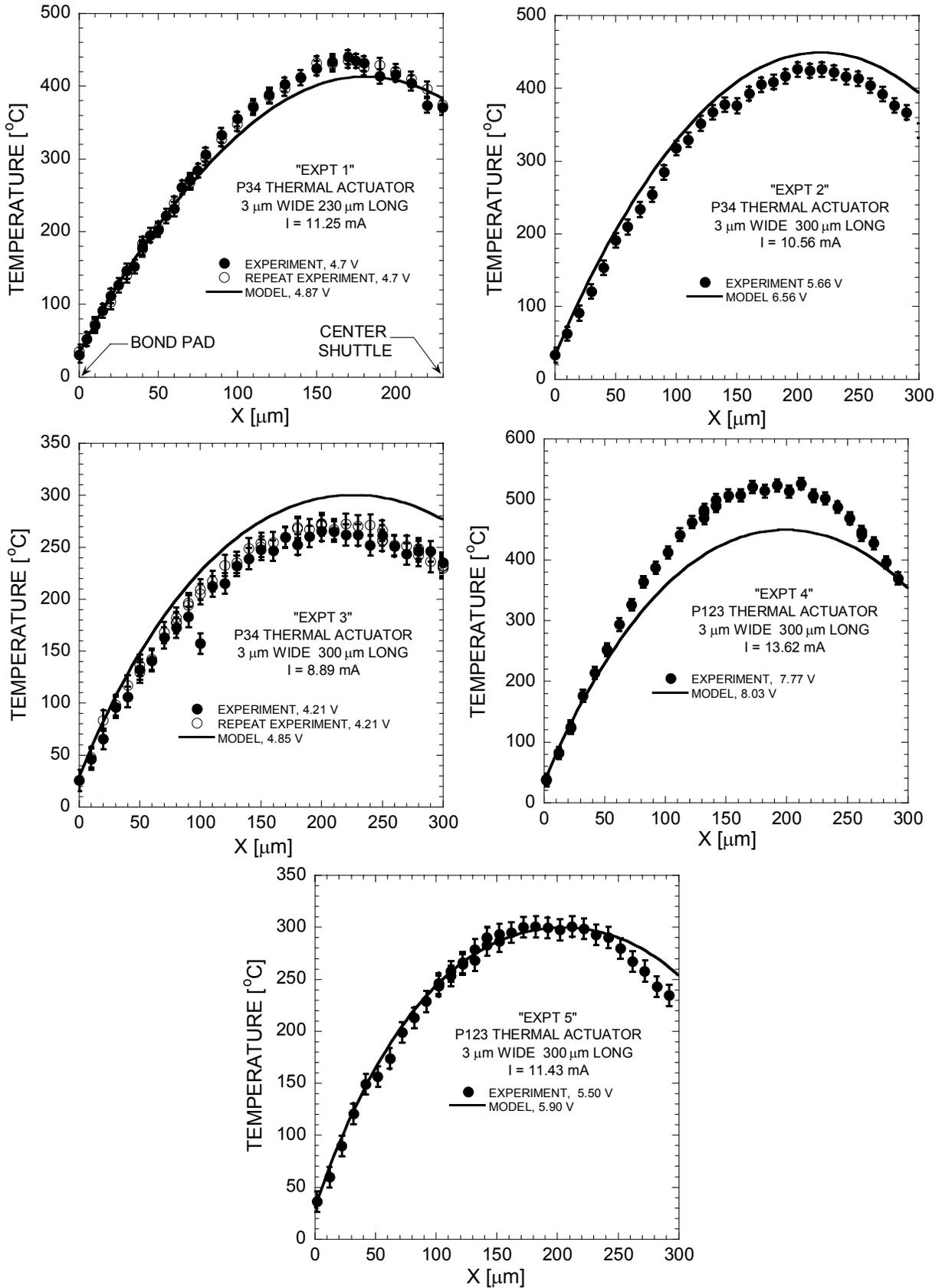
Figure 11 – Raman-measured and modeled temperature profiles for the five experimental configurations described in Table 1.

which acts as a large heat sink. A nominally constant peak-temperature region is then achieved at about 60-80% of the length of the actuator beam, followed by a more shallow decline in temperature closer to the actuator's center shuttle. The maximum temperature on the actuator beams is a critical parameter for ET actuator reliability, and the measured peak-temperature location is consistent with the observed hot spot during actuator testing [4]. The spatial resolution of the Raman technique allows temperature gradients of order 3000-4500 K/mm to be measured in the vicinity of the actuator bond pad. Repeat tests were conducted for experiments 1 and 3 on different days that were separated by several weeks. The Raman temperature data from these repeat tests were in agreement within the ±10-11 K uncertainty in the data (see Section 6) as indicated by the error bars in the plots for experiments 1 and 3.

The Raman data are compared to predicted temperature profiles obtained from a detailed thermo-mechanical model of actuator performance developed by Baker *et al.* [4]. The applied current and the measured and predicted actuator voltage drops are supplied in the plot legends. The modeled voltage drop is 3 to 16% higher than the measured values, indicating a slight overprediction of device power consumption. Agreement between measured and predicted temperatures is generally good for experiments 1, 2 and 5, while larger discrepancies between model and experiment are observed for experiments 3 and 4.

A quantitative comparison between model and experiment, based on the magnitude and location of the maximum actuator temperature, T_{max}, is presented in Table 2. The best agreement is achieved for the case of experiment #5, with less than 1 K difference between model and experiment. The worst-case scenarios in experiments 3 and 4 show disagreements in maximum actuator temperature of 28 and 76°C, or 11 and 15% of the characteristic temperature difference between the minimum, T_{min}, at the bond pad and T_{max} in each case. Prediction of the location of

Table 2 – Comparison between Raman-measured and modeled V-shaped actuator thermal performance.

EXPT. #	MEASURED T_{max} [$^{\circ}$C]	PREDICTED T_{max} [$^{\circ}$C]	DIFFERENCE [% OF TEMP. RISE]	TEMP. RISE $T_{max} - T_{min}$ [$^{\circ}$C]	MEASURED LOCATION OF T_{max} [μm]	PREDICTED LOCATION OF T_{max} [μm]
1	440	413	6.5%	410	170	182
1a	435	413	5.5%	400	170	182
2	426	450	5.9%	393	220	217
3	265	300	14.5%	240	200	225
3a	272	300	11.1%	247	200	225
4	526	450	15.6%	489	212	197
5	300	300	0.3%	264	212	205

maximum actuator temperature is within 3 to 25 μm, or 1 to 8% of the actuator beam length, when compared to experiment.

Chief sources of variability in the predicted temperature profiles are the temperature-dependent thermal conductivity and electrical resistivity of SUMMiT-V polysilicon and uncertainty in the device geometry as a result of finite tolerances in the SUMMiT-V fabrication process. For experiments 1, 2, and 5, the differences between model and data were found to be within the expected variability caused be geometric tolerances, while the differences for test cases 3 and 4 could not be attributed solely to geometric uncertainty [42].

5.1.4 Comparison to IR-Imaging Measurements

The degree of spatial resolution afforded by the Raman technique was found to be superior to what is attainable from earlier results obtained by mid-infrared imaging [4]. A mid-IR image of a P123-design, V-shaped electro-thermal actuator, typical of those probed in our Raman studies, is provided in Fig. 12. This IR image suggests that the heated region extends well beyond the body of the actuator and onto the surrounding substrate, an effect that was not anticipated. We expect some "blurring" of the IR image results, which can be estimated from the relative diffraction limits of the Raman and IR techniques. For collection optics of similar aperture, we can expect the relative spatial resolution to scale as $\lambda_{IR}/\lambda_{Raman} \sim 4$ μm / 0.488 μm = 8.2, where the λ represent the wavelengths of the Raman probe laser and the center of the 3-5 μm IR detection band. For an in-plane spatial resolution of 1-1.2 μm in the Raman measurements, we estimate a spatial resolution of 8-10 μm in the IR data. This is clearly too coarse to resolve the 3-μm-wide actuator leg features, which are then spatially averaged with the surrounding substrate.

As a check, a silicon Raman spectrum was recorded from the actuator substrate, with the Raman probe displaced ~10 μm from a P34-design actuator leg, into a region that the IR data indicated to be at elevated temperature. The substrate spectrum provided in Fig. 13 shows a narrow Stokes-side peak near 520.4 cm^{-1} and no detectable anti-Stokes signal, both of which indicate a room-temperature substrate, in disagreement with the IR-based predictions. The broad, featureless background in the substrate Raman spectrum is generated in the amorphous silicon nitride (0.8 μm thick) and thermal oxide (0.6 μm) substrate layers, while the well-defined Stokes-shifted Raman peak originates from the upper 400-600 nm of the single-crystal-Si wafer that supports these amorphous substrate films [31]. In this manner, the Raman peak in Fig. 13 is an indicator of the average temperature within the substrate at ~ 1.4–1.9 μm depth. However, the substrate is expected to be nearly isothermal throughout it thickness because the thermal

32

resistance of the low-conductivity actuator-to-substrate air gap is much larger than the resistance of the substrate materials.

5.1.5 V-Shaped ET Actuator Conclusions

Surface Raman scattering of laser light has been used to measure temperature profiles along a single beam of several V-shaped electro-thermal actuators within an uncertainty of ±10 K. The 1.2-μm in-plane resolution of our Raman probe is capable of resolving the 3-μm width of the actuator beams, which previous IR imaging measurements were not capable of providing. Measured temperature profiles for five different actuator scenarios are reported and compared to thermo-mechanical model predictions by Baker *et al.* [4]. Predicted maximum actuator temperatures are generally within 20-35 K of Raman data for measured characteristic device-temperature differences ranging from 240 to 410 K. A maximum deviation of 76 K between model and experiment, or 15% of the characteristic temperature rise, was observed in one case. To our knowledge, these are the first reported quantitative and spatially resolved temperature data from working MEMS thermal actuators. The data are useful for validation of most any thermal model of actuator performance.
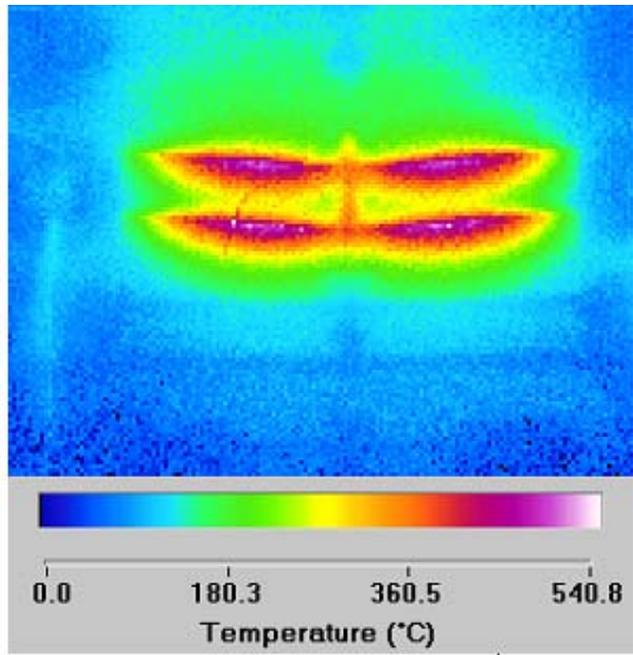
Figure 12 – Infrared image of a SUMMiT-V-fabricated V-shaped thermal actuator [4]. The image data suggest that the base layer surrounding the actuator has been heated.
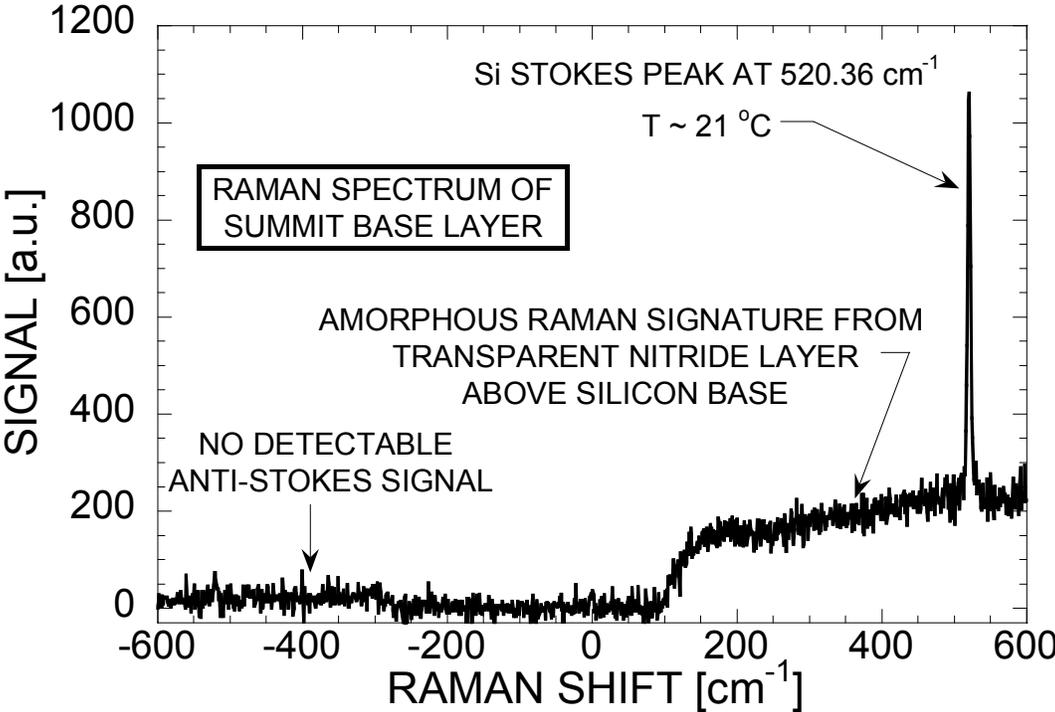
Figure 13 – Raman spectrum of a SUMMiT-V base layer. The spectrum was recorded with the Raman probe volume positioned slightly off of the leg of a V-shaped actuator of the type shown in the infrared image of Fig. 12. This spectrum shows no detectable anti-Stokes signal and a Stokes-shifted peak near 520.4 cm^{-1}, which is consistent with a room-temperature base layer.

5.2 SUMMiT-V-Fabricated Flexure-Style Thermal Actuators

5.2.1 Background

Electro-thermal actuators have become one of the most common elements of MEMS design in recent years. These actuators, which are based on thermal expansion of heated members, offer significant advantages over electrostatic actuators, including lower operating voltages and improved force and displacement characteristics [43]. There are two general types of electro-thermal actuators: the bent-beam or linear design, and the U-shaped or flexure design [4, 34, 35, 44-49]. In general, these actuators amplify the motion resulting from the thermal expansion of structural members as they are Joule-heated by a current flowing through the device. The versatility and usefulness of these devices has prompted the development of numerous models to predict and assess the actuator performance [37, 48, 49]. Because the devices operate using thermal expansion, their performance is invariably linked to the temperature profile produced during Joule heating, which, until recently, has not been experimentally verified [40]. The micron-scale dimensions of the devices mean that typical thermometry methods, such as infrared (IR) imaging, are incapable of providing adequate spatial and thermal resolution.

Here, we present the first spatially resolved temperature measurements of electro-thermal flexure actuators in operation by using micro-Raman spectroscopy. We compare the measurements to numerically obtained temperature profiles of similar devices from the literature, as well as to profiles obtained with our own numerical model of the particular devices under study. By tightly focusing a 488-nm-wavelength Ar^+ laser beam to a micron-scale probe spot and correlating the observed spectra of the probed region to the calibrated Raman response for polycrystalline silicon, micron-scale spatial resolution in the temperature measurement is obtained. Because photon collection times for any particular location on the device are on the order of a minute, only steady state temperature measurements are currently feasible.

5.2.2 Flexure-Type Actuator Design

The electro-thermal actuators used in this study consist of a polysilicon structure of the U-shaped, or flexure, design as shown in Fig. 14. The actuators have a thin "hot" leg and a wider "cold" leg joined at one end and are anchored to the substrate at the other. In operation, current flows through the polysilicon structure and causes greater heating within the hot leg due to its smaller cross section. The higher temperature attained in the thinner leg leads to dissimilar thermal expansion between the two legs and results in a rotary motion at the free end of the
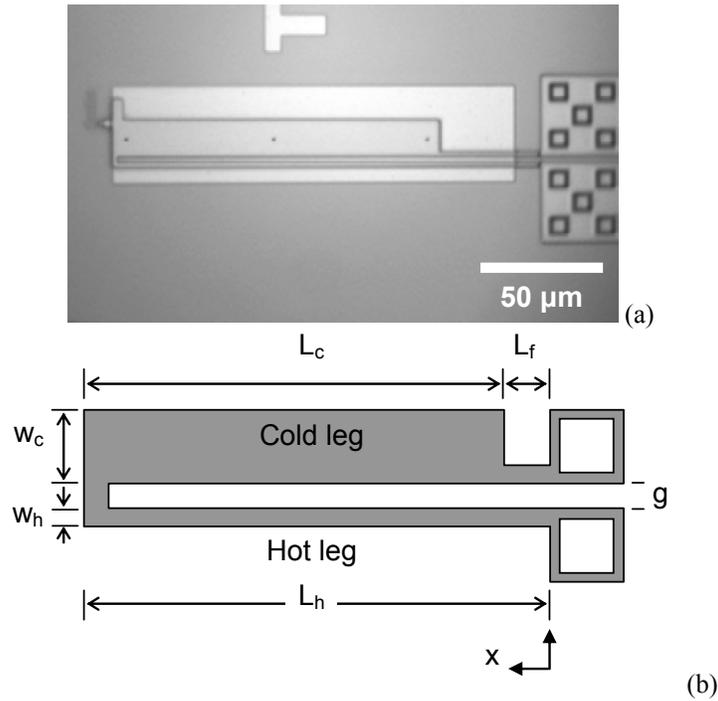
Figure 14 – (a) Image of a tested thermal flexure actuator. (b) Schematic diagram of a typical thermal flexure actuator showing critical dimensions for the actuator design.

actuator. Two different actuator geometries were tested as listed in Table 3. Three separate thermal actuators were powered by a current source between 1.5 and 2.5 mA.

The polysilicon MEMS actuators were fabricated using Sandia National Laboratories' SUMMiT-V™ (Sandia's Ultra-planar Multi-level MEMS Technology) process [31], which uses four structural polysilicon layers and a polysilicon base plane. Each structural layer is separated by a sacrificial oxide layer. After the final deposition, the oxide layers are etched away to release the polysilicon structure. The polysilicon layers are named Poly0-Poly4, in ascending order above the substrate. The base layer of polysilicon, Poly0, is 300 nm thick, while the structural layers vary in thickness from 1.0 μm for Poly1 to 1.5 μm for Poly2 and 2.25 μm for Poly3 and Poly4. The actuators used in this study were fabricated from a laminate of Poly1 and Poly2 for a nominal thickness of 2.5 μm and are designed to be 2.0 μm above the substrate. The parameters of significance in flexure-actuator design are labeled in Fig. 14b.

5.2.3 Flexure Actuator Experiments

A Stokes-peak-position-based temperature at the probed position is obtained using Eqs. 14. The peak-position-based temperature data shown in Fig. 15 represent the average of five Raman realizations at each point along the unfolded length of the actuator. The horizontal-axis origin in

Table 3 – Design dimensions of tested flexure-type actuators.

Actuator design	Hot leg length, L_h	Hot leg width, w_h	Cold leg length, L_c	Cold leg width, w_c	Flexure length, L_f	Leg separation distance, g
TA1	200 μm	2 μm	160 μm	15 μm	40 μm	2 μm
TA6	210 μm	2 μm	160 μm	18 μm	50 μm	3 μm

Fig. 15 is located at the base of the hot leg and extends along the length of the hot leg, around and along the cold leg, up to the base of the cold leg. All profiles for the different actuator designs show a similar trend. The temperature increases sharply along the hot leg up to the midpoint in the leg length and decreases as the position approaches the cold leg. As expected, the temperature rise along the cold leg is minimal in comparison with the hot leg, and forms the basis for the functionality of this type of device. Beyond the cold leg is the thin flexure element, which is similar in cross section to the hot leg and, therefore, also undergoes a slight temperature increase. The measured peak-position-based temperature profiles are in qualitative agreement with published numerical and analytical models for similar devices [35, 48, 49]. Deflection values for a TA6-design actuator powered at 1.5, 2.0, and 2.5 mA were 1.25 μm, 2.25 μm, and 4.75 μm, respectively.

Peak device temperatures depend on the driving current, vary from ~110°C at 1.5 mA to ~450°C at 2.5 mA, and are always located at the midpoint of the hot leg. For this reason, this location is the most likely failure point of the device as the current is increased. Greater currents will lead to even higher peak temperatures that are near the levels where polycrystalline silicon can plastically deform [50, 51]. Moreover, the increased thermal expansion in the hot leg with respect to the cold leg places the hot leg under compression which increases the potential for buckling of this thin and narrow structural member. Indeed, greater currents than the maximum used for the repeated measurements lead to permanent deformation of the hot leg and decreased actuator performance.

Bending in the flexure actuator mechanism results in levels of mechanical stress that are large enough to influence the Raman peak position. Fig. 16 shows temperature profiles of a TA6-design actuator obtained from both linewidth- and Stokes-peak-based measurements. The profiles show qualitative agreement with each other, with some scatter in the linewidth-based temperature data over the cold region. The scatter is representative of the uncertainty of the linewidth measurement. Neglecting the scatter in the cold-leg linewidth-based temperature, the profiles deviate most near the flexure points, i.e. near the bond pad and the leg joints, where the
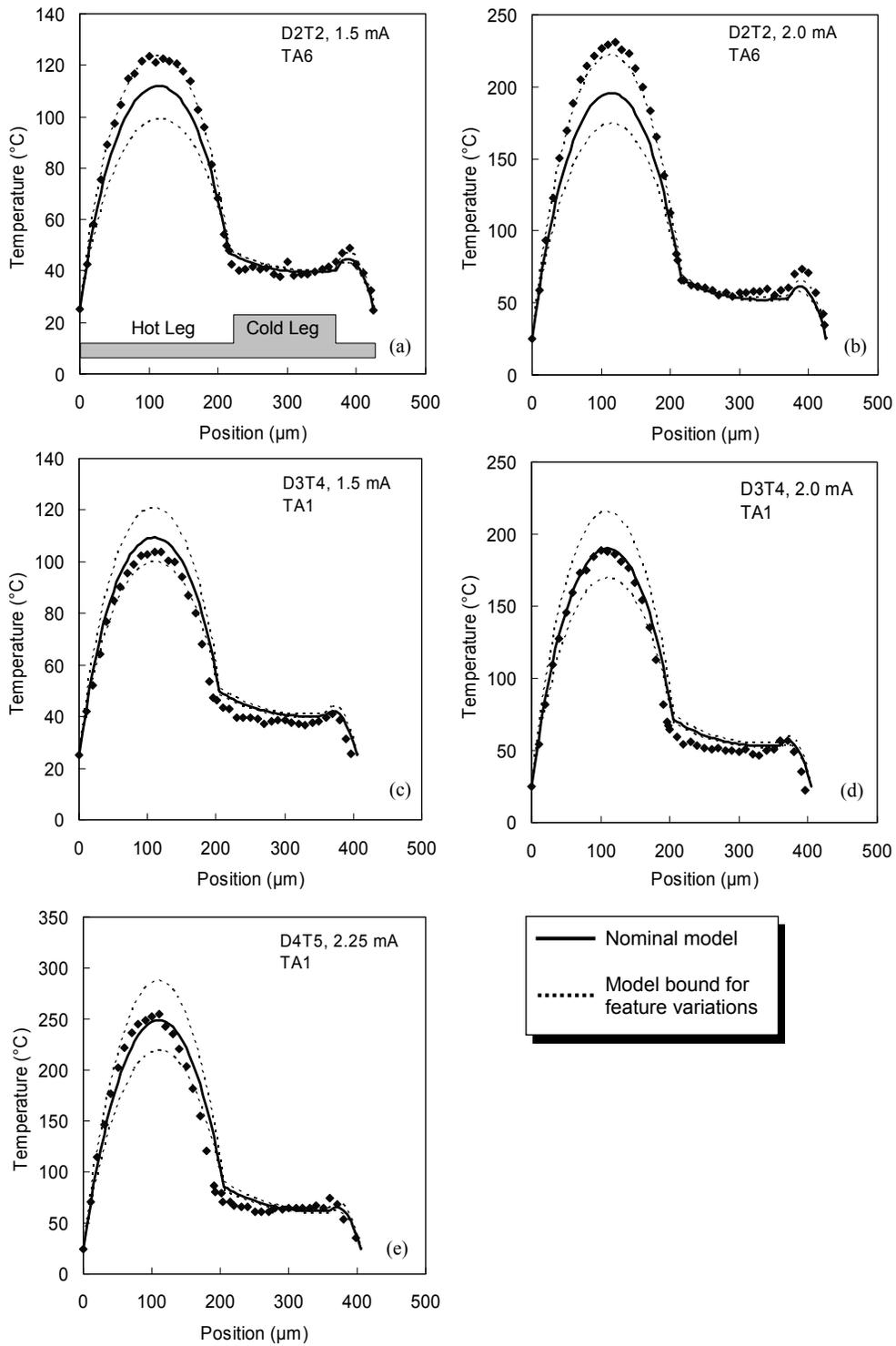
Figure 15 – Measured temperature profiles for U-shaped flexure-style thermal actuators along the unfolded length of the actuator as depicted in (a). The temperatures were obtained from Si Raman spectra using the Stokes-shifted peak position as a metric. The solid lines represent profiles obtained from a numerical model using the nominal actuator dimensions; dotted lines are profiles at the upper and lower extremes of the feature-width variations of fabricated SUMMiT-V devices.
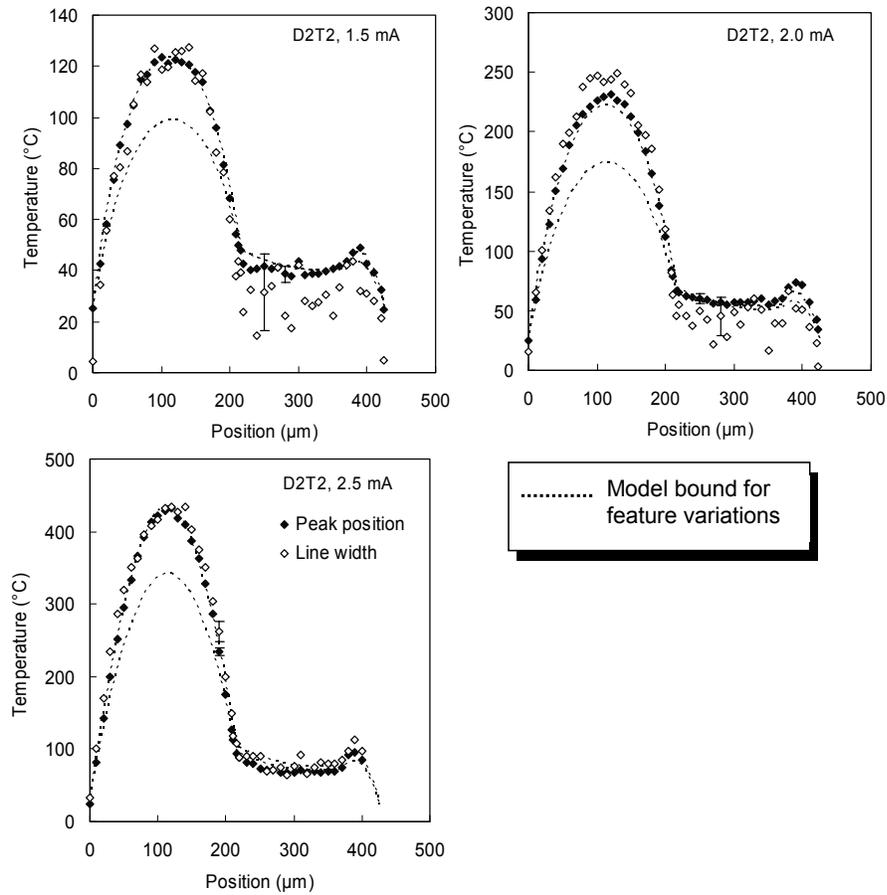
Figure 16 – Temperature profiles for a TA-6-design thermal actuator, as obtained from the Stokes-shifted Raman peak position (solid symbols) and the measured linewidth of the Stokes-shifted peak (open symbols). Error bars indicate relative uncertainty in temperature measurement for both techniques.

bending stress in the device is concentrated, and the peak-position-based measurement is generally higher than the linewidth-based temperature. The deviation in some regions is as high as 30°C, which is greater than the uncertainty in the peak-position-based temperature, and is likely due to stress-induced bias in the peak-position-based temperature. Because of the lateral bending of the structure, there can be a stress gradient along the width of the bending elements, and the magnitude of the bias in the peak-based measurement will depend on the position of the probe beam along the width of the leg. While free of stress-induced bias errors, the linewidth-determined temperature is not as robust as with the peak-position method, and has a precision error (scatter) in the temperature determination of up to ±15°C at elevated temperatures for a five-spectrum average.

5.2.4 Flexure Actuator Electrothermal Model

The measured temperature data are further compared to predicted temperature profiles obtained from numerical simulations of the actuators. We consider a simple one-dimensional heat-transfer model of the unfolded structure using an explicit finite-difference calculation. Although subject to stability requirements, this method allows for straightforward incorporation of temperature-dependant properties. Using a 1-D model is acceptable since typical flexure actuators have a high length-to-width aspect ratio, so that the lateral heat flow will have a minor impact on the overall device temperature. At the base of the actuator legs are the bond pads which are assumed to serve as heat sinks, such that the temperature at the base of the actuator legs is the same as the substrate temperature.

The finite-difference model, which follows the approach taken by Lott *et al.* [37], consists of dividing the unfolded device into discrete volume elements of equal length, and uniform temperature. For each element, a time-dependant heat-transfer equation is written which considers heat generation due to Joule heating (Q_J), heat conduction to and from adjoining elements (Q_{i-1} and Q_{i+1}), heat conduction to the substrate (Q_C), heat loss through radiation (Q_R), and heat accumulation (Q_S). At each time step energy balance requires that:

$$Q_S = Q_J + Q_{i-1} + Q_{i+1} + Q_C + Q_R \qquad (16)$$

Our model ignores free-convection heat transfer since the Rayleigh number, based on the actuator's hydraulic diameter, is of order 10^{-7} to 10^{-8}. Fluid motion in the vicinity of the actuator is very small, and heat loss from the structure is dominated by conduction through the high temperature gradients in the vicinity of the actuator.

Each contribution in Eq. 16 can be expressed as follows.

a. Joule heating, Q_J:

$$Q_J = J^2 \rho_r(T) V_i \quad , \qquad (17)$$

where J is the current density flowing through the volume element, $\rho_r(T)$ is the temperature-dependant resistivity of the polysilicon, and V_i is the discrete volume element.

b. Heat conduction, Q_{i-1} and Q_{i+1}:

$$Q_{i-1} = \frac{1}{2}\frac{A_x}{\Delta x}\left[k_p\left(T_{i-1}^j\right) + k_p\left(T_i^j\right)\right]\left[T_{i-1}^j - T_i^j\right] \quad , \tag{18}$$

$$Q_{i+1} = \frac{1}{2}\frac{A_x}{\Delta x}\left[k_p\left(T_{i+1}^j\right) + k_p\left(T_i^j\right)\right]\left[T_{i+1}^j - T_i^j\right] \quad , \tag{19}$$

where A_x is the cross sectional area of the element, Δx is the length of the element, $k(T)$ is the temperature-dependant thermal conductivity of the polysilicon, and T_i^j represents the temperature of the ith element at time step j.

c. Substrate conduction, Q_C:

$$Q_C = \frac{SA_u}{R_T}\left(T_{sub} - T_i^j\right) \quad , \tag{20}$$

where T_{sub} is the substrate temperature, and A_u is the surface area that faces the substrate. S is a conduction shape factor which can be expressed as [35, 37, 48, 49] $S = \frac{h}{w}\left(\frac{2h_{air}}{h} + 1\right) + 1$ for an element of height h and width w, at a distance h_{air} over the substrate. R_T is the equivalent thermal resistance of the combined air, oxide, and nitride layers between the silicon-wafer substrate and the polysilicon actuator, and is given by:

$$R_T = \frac{h_{air}}{k_{air}} + \frac{h_{SiO_2}}{k_{SiO_2}} + \frac{h_{Si_3N_4}}{k_{Si_3N_4}} \quad , \tag{21}$$

where h_X and k_X refer to the thickness and thermal conductivity of layer X, respectively.

d. Radiative Heat Loss, Q_R :

$$Q_R = (2h + w)\varepsilon\sigma\left[T_{sub}^4 - \left(T_i^j\right)^4\right] \quad , \tag{22}$$

Table 4 – Parameters for best model fit to measured flexure-type actuator temperature profiles.

Part ID	Actuator Design[a]	Hot leg width, w_h	Actuator thickness	Distance above substrate
D2T2	TA6	1.75 μm	2.4 μm	2.1 μm
D3T4	TA1	1.90 μm	2.45 μm	1.9 μm
D4T5	TA1	1.90 μm	2.4 μm	2.1 μm
[a] See Table 3 for design parameters				

where ε is the emissivity of heated polysilicon, and $\sigma = 5.670 \times 10^{-8}$ W/m^2-K^4 is the Stefan-Boltzmann constant.

e. Heat accumulation, Q_S:

$$Q_S = \frac{\rho c V_i}{dt}\left[T_i^{j+1} - T_i^j\right] \quad , \tag{23}$$

where $\rho = 2330$ kg/m^3 and c = 705 J/(kg °C) are the density and specific heat of polysilicon, respectively, and dt is the time increment. By substituting Eqs. 17–23 into Eq. 16 and applying the proper boundary conditions — bond pad temperature fixed at T_{sub} and initial temperature equal to T_{sub} everywhere — a numerical solution can be obtained for the temperature at time step *j+1*.

The model considers the temperature dependence of the thermal and electrical properties of the actuator material, as well as the geometry and dimensions of the device. For the SUMMiT-V structural polysilicon layers, the thermal conductivity up to 700°C can be expressed as [4],

$$k_p(T) = (-2.2 \times 10^{-11} T^3 + 9.0 \times 10^{-8} T^2 - 1.0 \times 10^{-5} T + 0.014)^{-1} \quad . \tag{24}$$

Likewise, the resistivity can be computed from [4],

$$\rho_r(T) = \begin{cases} 2.9713 \times 10^{-2} T + 20.858, & T < 300°C \\ 6.1600 \times 10^{-5} T^2 - 7.2473 \times 10^{-3} T + 26.402, & 300°C < T < 700°C \end{cases} \quad . \tag{25}$$

In Eqs. 24 and 25, k_p is in units of W/m-K, ρ_r is in units of $\Omega-\mu$m, and T is expressed in degrees centigrade.
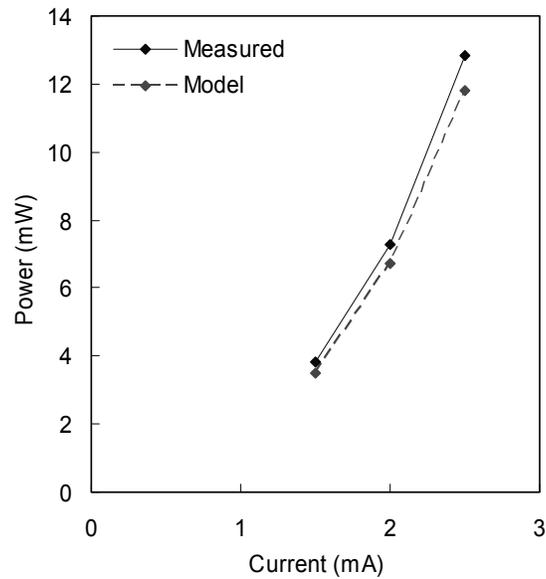
Figure 17 – Comparison of the measured and modeled power dissipation for thermal actuator part D2T2 operated at current from 1.5 mA to 2.5 mA. The model results are based on the best-fit geometry listed in Table 4.

The solid lines in Fig. 15 show the result of modeling actuators of nominal fabricated dimensions, i.e. typical fabricated device dimensions for the given as-designed dimensions listed in Table 3. The agreement between data and nominal model appears to be device dependant and could be indicative of processing variations in the device fabrication. SUMMiT-V processing typically results in features that are 0.10 ± 0.08 μm per edge smaller than as-designed. Along the 2-μm-wide hot leg, this variation amounts to ~20% change in the width and can result in significant variation in the modeled temperature profiles as indicated by the dotted lines in Fig. 15. In general, the measured temperature profiles lie within the error bands associated with SUMMiT-V process width variations.

By adjusting the modeled geometry within the known process variations, we were able to obtain best fits to the measured temperature data. Best-fit geometric parameters are listed in Table 4. Variations in the actuator thickness are within the part-to-part variations for SUMMiT-V processing of Poly12 laminate, which results in films 2.50 ± 0.1 μm in thickness. In addition, the variation in the distance to the substrate is accounted for by the part-to-part variation in the sacrificial oxide layer under the actuator, which is ± 0.10 μm. The modeled profiles using these parameters are generally within $\pm 10°$C of the measured temperature values. The prediction of the power dissipation for the best-fit model is within 8% of the measured value, as shown by the results for part D2T2 in Fig. 17. The actuator model does not include the electrical impact of the bond pads or the length extension of the structure from thermal expansion, both of which can increase the total device resistance and cause an underprediction of the dissipated power.

5.2.5 Flexure Actuator Conclusions

Micro-Raman scattering has been used to measure the temperature profiles along the length of U-shaped electro-thermal actuators. The sub-micron diameter of the Raman probe allowed the profile along the 2-μm-wide hot leg to be resolved. The measured profiles are the first set of direct measurements on active flexure-type actuators, and are in qualitative agreement with published numerical models of similarly-shaped actuators and within reasonable quantitative agreement with numerical models of the geometry under study. In addition, we report the use of Stokes linewidth for thermometry purposes, which shows good agreement with Stokes-peak-position-based temperature measurements, while revealing some stress-induced bias in the peak-position-based temperatures. Peak position-based temperatures values were generally within ±10°C of the best-fit modeled temperature values.

5.3 GaN Transistor

5.3.1 Device Description

   In addition to silicon-based MEMS devices, Raman thermometry can also be used for thermometry on any Raman-active material. One example of Raman thermometry on materials other than Si is our study of a High-Electron-Mobility Transistor (HEMT), manufactured on a GaN layer with a 6H SiC substrate. The device has 20 source-drain pairs and can dissipate upwards of 20 W of power in DC operation. Figure 18a shows an optical image of the device tested, while Fig. 18b has a close-up of the probed region showing the source, drain and gate elements of a single transistor. The device is bonded to a 6.35-mm-thick copper heat spreader that also contains other electronic components associated with the transistor. The devices were tested under DC conditions at a gate voltage of -2.0 V, a drain voltage of 10.0V, and a drain current of 1.17 A. While the copper heat spreader helps in the thermal management of the device as a whole, the large thermal mass of the copper plate causes the device to take approximately 15–30 minutes to reach thermal equilibrium after powering. At thermal equilibrium, the temperature of the copper heat spreader is ~48°C, as measured with a thermocouple attached to the plate, and the drain current has lowered to 1.00 A.

5.3.2 Temperature Dependence of GaN and SiC Raman Spectra

   To correctly measure temperatures in GaN-based devices, the temperature response of the Raman spectrum of GaN must be known. The devices of interest are composed of a ~1.0-μm-thick layer of GaN grown on 6H SiC. Because the GaN layer is semitransparent at the Raman probe wavelength of 488 nm and the film thickness is small, the Raman spectrum of a GaN/SiC
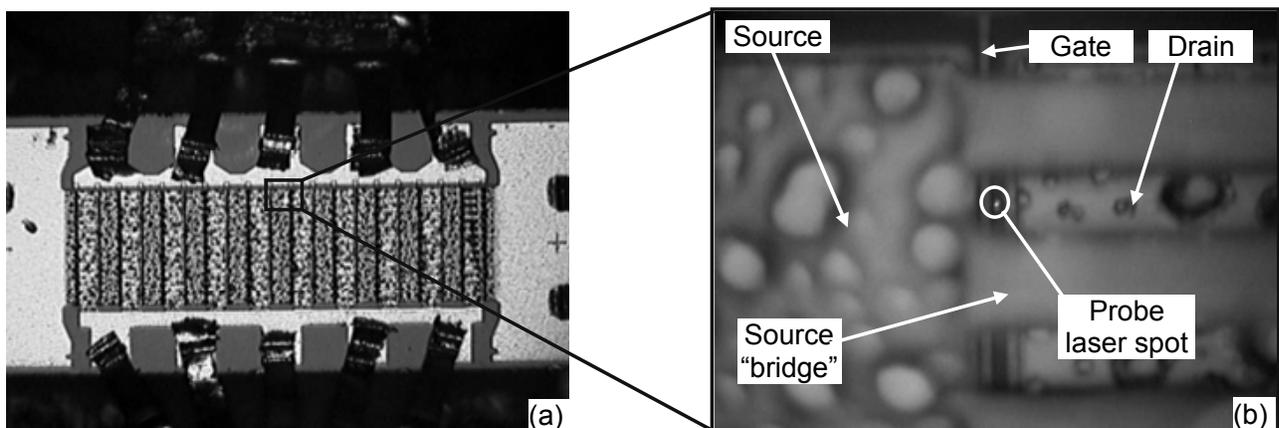
Figure 18 – Optical image of the GaN HEMT: (a) entire device, (b) close-up showing source, drain, and gate regions of the device as well as the Raman probe spot.
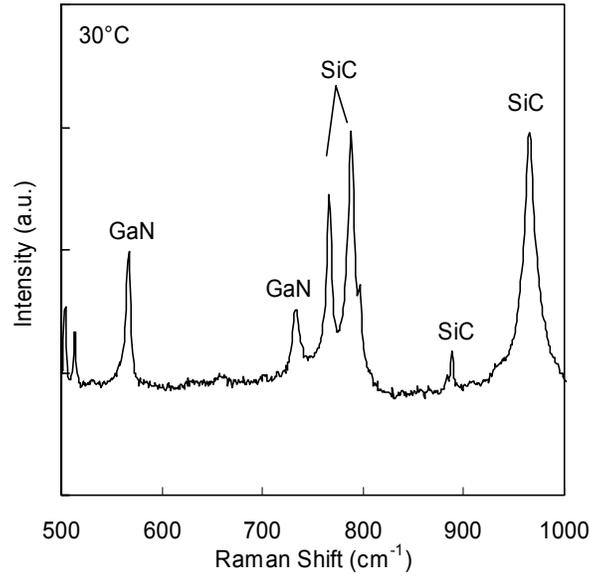
Figure 19 – Room-temperature Raman spectrum for a GaN film on SiC showing Raman peaks for the GaN film and the SiC substrate. The isolated peaks at ~565 cm^{-1}, corresponding to GaN, and at ~965 cm^{-1}, corresponding to SiC, are used for temperature calibration.

sample presents peaks corresponding to both materials, as shown in Fig. 19. Major peaks are observed in the vicinity of 565, 733, 766, 788, and 965 cm^{-1}. By obtaining spectra from a bare SiC sample, we can correctly identify which of the observed peaks correspond to which material; the peaks at 565 and 733 cm^{-1} corresponding to GaN and the other peaks resulting from the SiC substrate, as labeled in Fig. 19. The isolated peaks near 565 cm^{-1} and 965 cm^{-1}, corresponding to the E2 and LO phonon modes in GaN and SiC, respectively, are best for calibrating the temperature response of GaN and SiC.

The calibration is done by placing samples in a controlled-temperature hot stage (Linkam TS1500) and capturing spectra at 50°C intervals from 30°C to 600°C. At each temperature step, five spectra, each averaged for 30 seconds or more, are captured and analyzed to extract the position and linewidth of the diagnostic Raman peaks. The results for each temperature step are averaged and used for temperature calibration. The temperature dependence of the diagnostic Raman spectra is shown in Fig. 20 for both the GaN and SiC peaks. Like the changes observed in the Raman spectrum of silicon, the Raman peaks for both materials broaden and shift in position relative to the room-temperature peak.

Figure 21 shows the temperature evolution of the Raman shift, Ω, for the diagnostic peaks between 30°C and 600°C, for both materials. The dotted lines represent a fit of the data to the empirical equation,
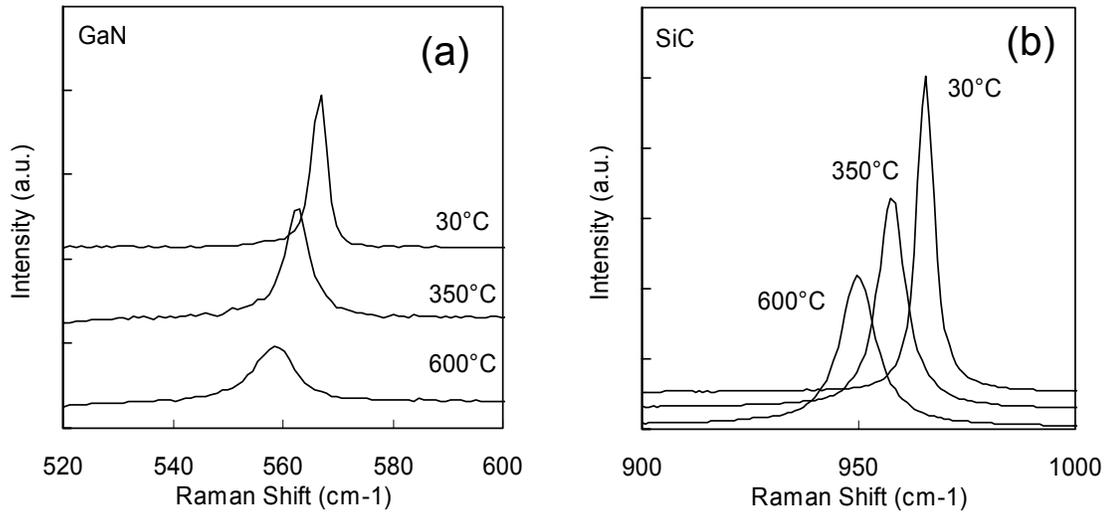
Figure 20 – Isolated Raman peaks for temperature calibration of (a) GaN and (b) SiC. Spectra are shown at varying temperatures to illustrate changes in Raman peak position and linewidth.

$$\Omega = A(T - B)^2 + C \quad , \tag{26}$$

where A, B, and C are fit constants with the values shown in Table 5.

Like the peak position, the linewidth of the Raman peaks also changes with temperature, as shown in Fig 22, and can also be described by a quadratic empirical equation,

$$\Gamma = a(T - b)^2 + c . \tag{27}$$

Although either the peak position or the linewidth can be used for temperature-diagnostic purposes, the determination of the linewidth results in greater temperature uncertainty than the determination of the peak position. The result is an uncertainty of ±7°C for the peak-position-

Table 5 – Empirical constants from Eqs. 26 and 27 for the temperature response of the GaN and SiC Raman-diagnostic peaks.

	Ω (cm^{-1})			Γ (cm^{-1})		
	A	B	C	a	b	c
GaN	-7.78×10^{-6}	-660.15	570.69	1.29×10^{-5}	-79.49	2.979
SiC	-2.148×10^{-5}	-371.74	969.27	4.623×10^{-6}	-77.55	1.826
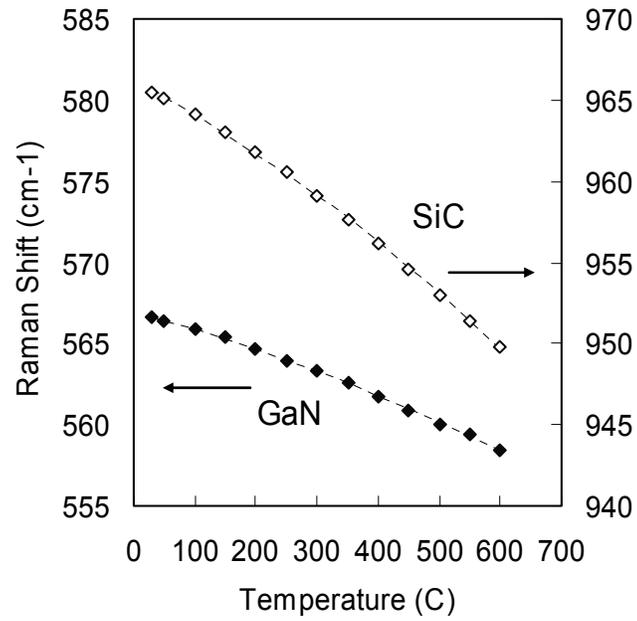
Figure 21 – Temperature dependence of the Raman shift of the E2 phonon mode of GaN and the LO phonon mode of SiC. The dotted lines represent least-squares fits to the data using Eq. 26.
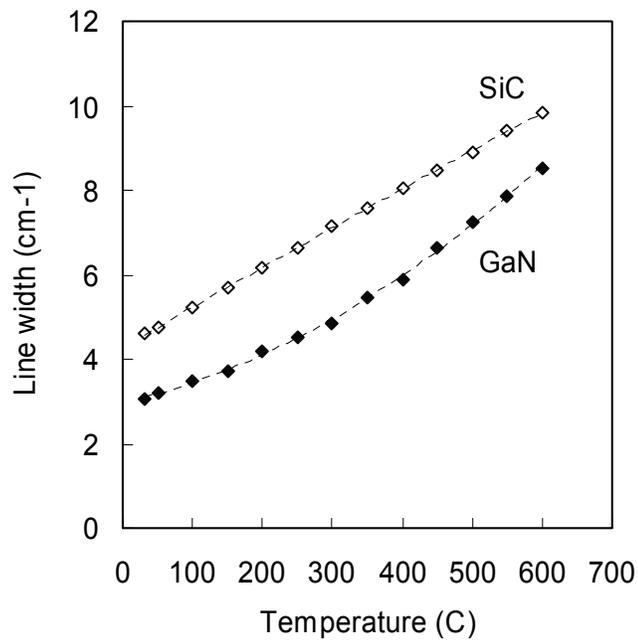
Figure 22 – Temperature dependence of the measured linewidth of the E2 phonon mode of GaN and the LO phonon mode of SiC.

based temperature calibration, compared to ±11°C for the linewidth-based calibration, both of which apply for temperatures obtained from the average properties of five Raman measurements.

5.3.3 Measurement Results

Since the GaN is semitransparent to the 488-nm probe wavelength, the Raman spectrum of portions of the device without metallization (region between the source and the gate and between the gate and the drain) contain information corresponding to both the top GaN layer as well as the SiC substrate. For diagnostic purposes, the Raman peaks near 565 cm^{-1} and 965 cm^{-1}, corresponding to the E2 and LO phonon modes in GaN and SiC, respectively, are used to probe the device temperature.

The region between the gate and the drain along the transistor was probed, as shown by the position of the probe-laser spot in Fig. 18b. Probing in the narrower gate-source space was affected significantly by the overlying metallization and positional drift of the part caused by the slow heating of the device. In the device tested, the sources in each transistor line are connected through a series of metallized bridge-like structures spaced ~10 μm apart and along the length of the device as indicated in Fig. 18b. To minimize overstressing of the device and minimize the measurement time, the temperature was measured at the center of the alternating spaces between the source bridges, approximately 78 μm apart. Only the transistor line at the center of the device, as shown in Fig. 18a, was measured. By being farthest from the outside of the device, this region is expected to suffer the greatest temperature increase.

Five Raman spectra were captured at each point using an incident laser power of 500 μW, and an integration time of ~30 s for each acquisition. Each spectrum was analyzed by fitting the measured spectrum to the Voight function of Eq. 13 to determine the location and width of the diagnostic Raman peaks for GaN and SiC. The resulting metrics for the five spectra at each point are then averaged and converted using the temperature response of the respective peaks shown in Figs. 21 and 22. As shown in Fig. 23, the temperature measured across the device, when powered at a drain voltage of 10.0 V and a drain current of 1.00 A, is approximately 150°C, as determined from both the GaN and SiC peak locations. While the Raman probe can penetrate into the SiC substrate and obtain a temperature measurement from a deeper portion of the device, the thermal gradient in the device is minimal, as evidenced by the ~48°C copper heat spreader temperature, and the temperature in the probed SiC volume is very close to the GaN temperature.
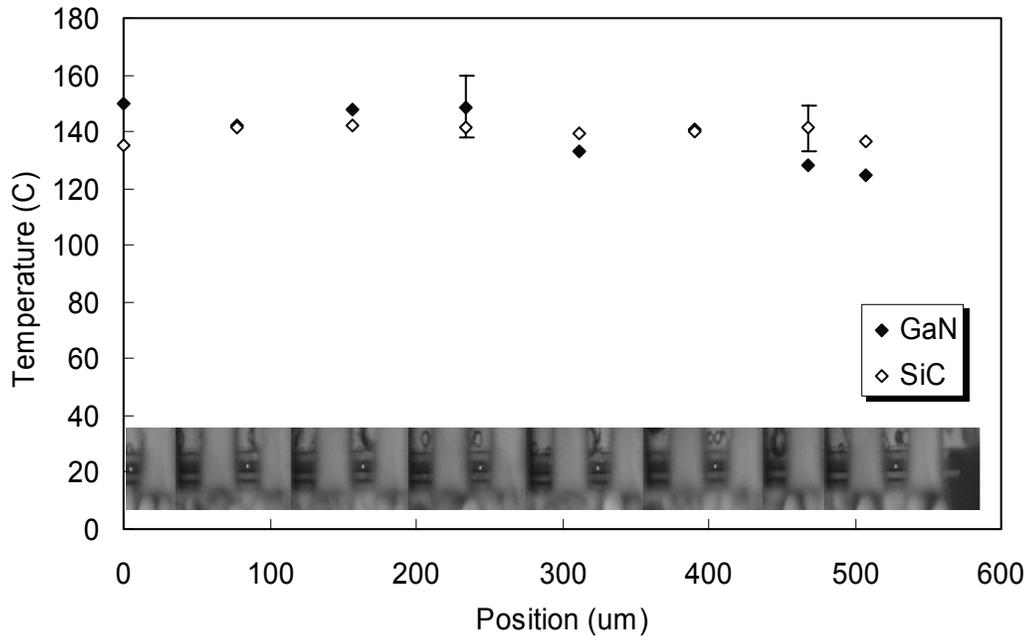
Figure 23 – Temperature across a GaN transistor, powered at a drain voltage of 10.0 V and a drain current of 1.00 A, as determined from the location of the Raman peaks corresponding to the E2 phonon mode in the GaN layer (closed symbols) and the LO phonon mode in the SiC substrate (open symbols). Error bars indicate the uncertainty estimate in the temperature determination for each material.

In addition to measuring the temperature along the length of the device, the temperature was probed along the width of the gate-drain junction shown in Fig. 24. The Raman probe laser was moved in 0.5-μm increments along the ~1.5-μm-length junction. Like the previous profile measurement, five spectra were captured at each point and analyzed to extract peak location information for both the GaN layer and the SiC substrate. The temperature data shown in Fig. 25 indicate that the temperature near the drain is ~150°C like the previous measurements. Near the gate, however, the measured temperature is closer to ~160°C. Since this region should have the highest electric field gradient, the higher temperature in the region is expected [52, 53].

Previous IR-imaging measurements of the device temperature field, with the transistor operated at a DC power of 25.8 W, indicate a peak temperature of ~210°C at the gate-drain junction, as seen in Fig. 26a [54]. Temperatures averaged across the gate-drain junction for varying levels of dissipated power are shown in Fig. 26b. At a power dissipation of 22.6 W, the Raman-based junction temperature is ~320 °C, which is significantly higher than indicated by the IR data acquired at 14% greater dissipated power. These results illustrate the caution that must be used when interpreting IR-image data as already mentioned in Sections 1 and 5.1.4 of this report.
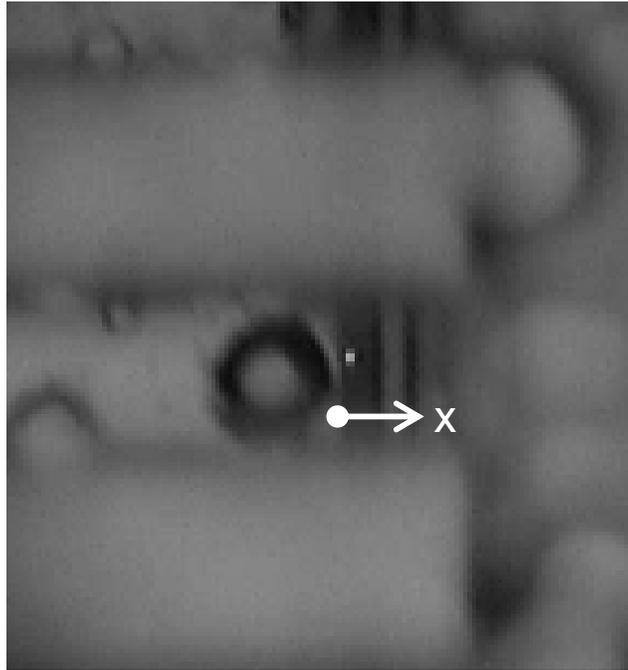
Figure 24 – Close up of gate-drain junction region probed with Raman spectroscopy.
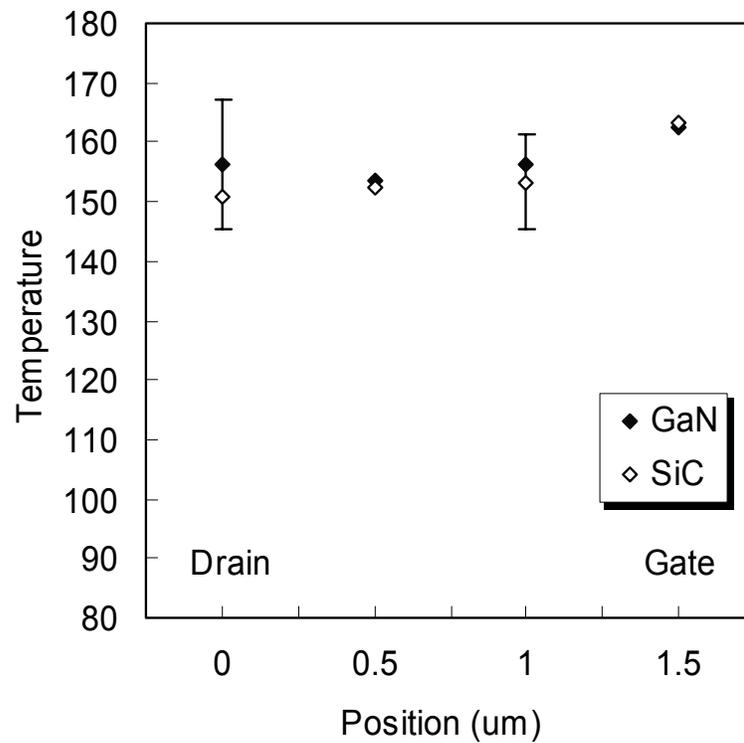
Figure 25 – Temperature profile along the gate-drain junction measured with Raman thermometry. The measured temperatures indicate a slight temperature increase in the region closest to the gate.
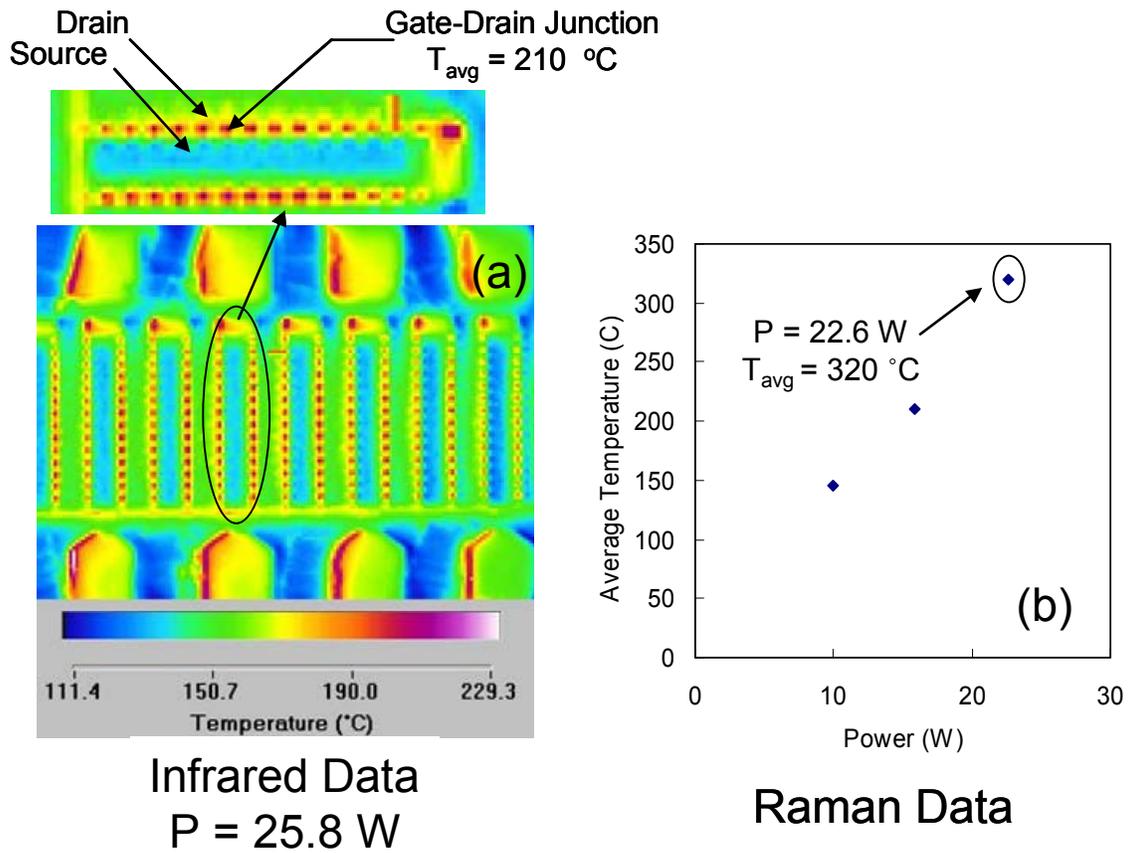
Figure 26 – Infrared image obtained from the GaN HEMT operated 25.8 W power dissipation (a). Raman-measured temperature, averaged across the gate-drain junction, as a function of dissipated power (b). At comparable power levels, the Raman-measured temperatures are ~ 110 ˚C higher than those measured with infrared.

6. UNCERTAINTY ESTIMATE FOR PEAK-POSTION-BASED RAMAN THERMOMETRY

An estimate of the uncertainty in the peak-position-based Raman-measured temperatures was obtained by individually considering the contributions of several key sources of error, which are listed in the left-most column of Table 6. The uncertainties in Table 6 are primarily the result of bias (systematic) errors, with the exception of the precision (random) error associated with the subpixel accuracy of the Voight curve fitting used to locate the Raman peaks. The values in Table 6 represent our best estimate of a 95% confidence interval in the component-level uncertainties, which were *vector* summed according to accepted methods of uncertainty quantification [55] to obtain total uncertainty estimates of ±10 K at room temperature and ±11 K at 700 K. This estimate is strictly valid for Raman thermometry of Si, and is based on a single realization of the Raman peak position at the low levels of stress encountered in the unconstrained V-shaped polysilicon thermal-actuator experiments reported in Section 5.1. Estimates for other materials will differ slightly, but are expected to be of the same order as for silicon.

The dominant source of uncertainty is alignment drift of the optical system, which causes up to a ±1 pixel (0.95 cm^{-1}) variation in the positioning of the spectral axis of the CCD detector over the course of a day. The impact of this drift was minimized by frequently recording reference spectra from samples at known ambient temperatures. Temperatures were deduced based on the relative change in peak location, as in Eqs. 14, which reduced the drift bias to about ±0.25 pixel, or ±9 K temperature-measurement uncertainty. This level of drift bias was a typical worst-case scenario and was often not as severe.

Detailed thermo-mechanical modeling by Baker *et al.* [4] has revealed that free-standing V-shaped thermal actuators can experience uniaxial stresses up to 100 MPa in either compression or tension. Stress has been observed to cause shifts in the Raman peak locations and Raman

Table 6 – Uncertainty estimates for peak-position-based thermal-actuator temperatures.

SOURCE OF UNCERTAINTY	UNCERTAINTY TYPE	PEAK LOCATION UNCERTAINTY	TEMPERATURE UNCERTAINTY
Accuracy of Peak Locator	PRECISION	±0.055 cm^{-1}at 300 K	±2.3 K at 300 K
		±0.095 cm^{-1}at 700 K	±4.1 K at 700 K
Instrument Drift	BIAS	±0.22 cm^{-1}	±9 K
Slope of Calibration Curve Fit	BIAS	±0.00016 cm^{-1}/K	±0.1 K at 300 K
			±2.7 K at 700 K
Laser-Induced Heating	BIAS	negligible	negligible
Axial Stress	BIAS	0.083 cm^{-1} (±100 MPa max. axial stress)	±3.5 K

scattering has been used as a stress-measurement diagnostic, where reports of stress-induced Raman shifts ranging from -1.8 to -4 cm^{-1}/GPa (hydrostatic) have been observed [12, 13, 19]. Using a nominal value of 2.5 cm^{-1}/GPa, a maximum stress-induced bias of ± 3.5 K was computed from the levels of hydrostatic stress, $\sigma_H = (\sigma_{xx} + \sigma_{yy} + \sigma_{zz})/3$, expected in the V-shaped thermal-actuator experiments.

The subpixel precision with which the Raman peak could be located from Voight curve fitting (Eq. 13) was determined by generating histograms of peak-location measurements from ensembles of 1000 Raman spectra under conditions similar to the experiment and reporting their 95% width, which ranged from 1/17 pixel at room temperature to 1/10 pixel at 700 K.

Goodness-of-fit measures of the confidence interval for the slope estimator of the linear fit to the polysilicon calibration data of Fig. 7 were used to estimate the impact of uncertainty in the Raman instrument calibration. Calibration errors ranged from ± 0.1 K at room temperature to a maximum of ± 2.7 K in the hottest portions of the actuators. A vector sum of the component uncertainties in Table 6 results in total uncertainties of ± 10 K at room temperature and ± 11 K at 700 K, which can likely be cut in half if an online absolute spectral reference is employed, such as Ar$^+$ plasma or calibration-lamp lines.

7. SIMULTANEOUS TEMPERATURE-STRESS MAPPING BY RAMAN SPECTROSCOPY

7.1 Background and Measurement Principles

Analysis of the Stokes-shifted Raman peak position has been used to estimate either temperature [9, 40, 56] or stress [12, 13] in microelectronics and MEMS devices. However, if the thermal and mechanical fields are evolving simultaneously, the Stokes-shifted peak location represents the impact of both quantities, making it difficult to measure either accurately. By using the independence of the measured linewidth to applied stress, it is possible to deconvolve the signal and obtain a simultaneous measure of both temperature and stress. A method is presented here where the temperature and biaxial stress were simultaneously measured in a doped polysilicon microheater. The data were acquired using a Renishaw Raman microscope at the Georgia Institute of Technology. This instrument is similar to the Sandia Raman microscope discussed in Section 3 of this report and its details are not presented here.

The temperature of a silicon sample, which experiences simultaneous heating and thermally induced stress, can be obtained from Raman peak-width data in conjunction with linewidth-temperature calibration results of the type shown in Fig. 8. For the range of temperatures considered, the linewidth data of Fig. 8 can be adequately fit using a quadratic polynomial, such that the linewidth-based temperature is obtained from,

$$T_\Gamma = \sqrt{\frac{\Gamma - C}{A}} - B \equiv T \quad , \tag{28}$$

where Γ is the measured linewidth in wavenumbers and T_Γ is measured in either Kelvins or degrees Centigrade, depending upon the choice of calibration constants A, B, and C. Since the measured linewidth is stress-independent, T_Γ is taken as a measure of the *true* value of the local temperature, T. Experimental confirmation of the stress-independence of the linewidth is given in Fig. 27a, where the measured linewidth for a polysilicon sample placed in a uniaxial bending stage is plotted against the applied bending stress. The results show no dependence of the linewidth on stress within the signal-to-noise in the data. This confirms the discussion of Section 2.2.2, in which the Raman peak width is expected to be primarily a function of the temperature-dependent phonon lifetime, and not strain-induced volumetric expansion.

Both temperature and stress impact the measured Stokes-shifted peak position. It has been shown in Fig. 7 that the Stokes shift in the Raman spectrum of an unconstrained silicon sample is
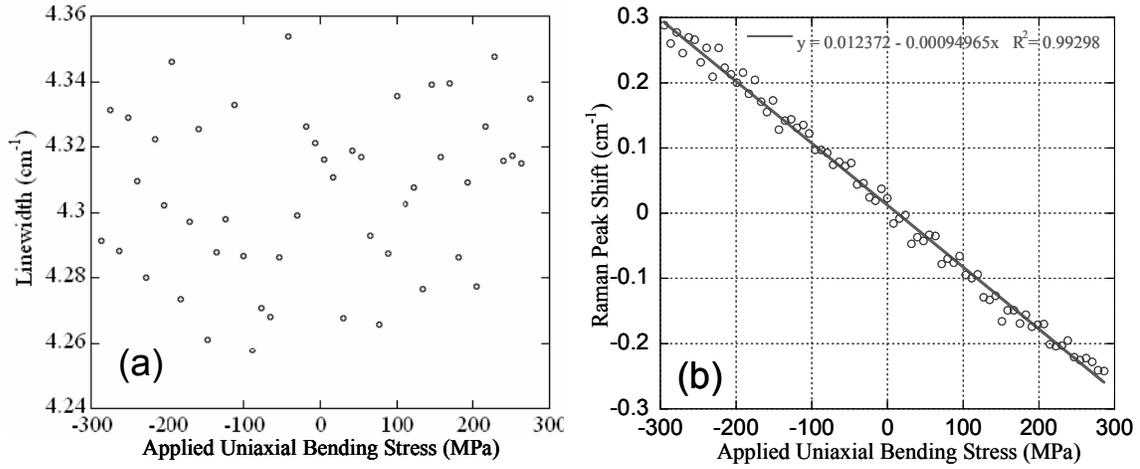
Figure 27 – Stress dependence of the measured linewidth (a) and position (b) of the Stokes-shifted Raman peak. The data were obtained from a polysilicon sample placed in a uniaxial bending stage at room temperature. The results show that the Stokes-side peak shift varies linearly with stress, while the linewidth is insensitive to stress

a linear function of temperature over a very broad range, such that a peak-position-based temperature can be obtained from a linear fit to the data,

$$T_\Omega = T_o + \left(\frac{\partial \Omega}{\partial T}\right)_\sigma^{-1} (\Omega - \Omega_o) \quad , \tag{29}$$

where T_o is the ambient lab temperature, $(\partial \Omega / \partial T)_\sigma$ is the slope of the stress-free peak-position versus temperature curve, and $\Omega - \Omega_o$ is the measured Stokes shift between device and ambient temperatures. Since stress impacts the measured Stokes shift, T_Ω is observed to be biased by the applied stress field. Isothermal bending experiments on silicon reveal that the magnitude of the stress-induced bias varies linearly with stress, as shown in Fig. 27b. The stress-induced bias in the measured Stokes peak position can be computed from,

$$\Omega_\sigma - \Omega_o = \left(\frac{\partial \Omega}{\partial \sigma}\right)_T (\sigma - \sigma_o) \quad , \tag{30}$$

where $\Omega_\sigma - \Omega_o$ is the stress-induced bias in the measured Stokes shift, $(\partial \Omega / \partial \sigma)_T$ is the slope of a linear fit to bending data of the type shown in Fig. 27b, and $(\sigma - \sigma_o)$ is the applied mechanical stress.

We can solve Eqs. 28 – 30 for the stress in the silicon sample by realizing that the measured Stokes shift is the sum of stress- and temperature-induced components,
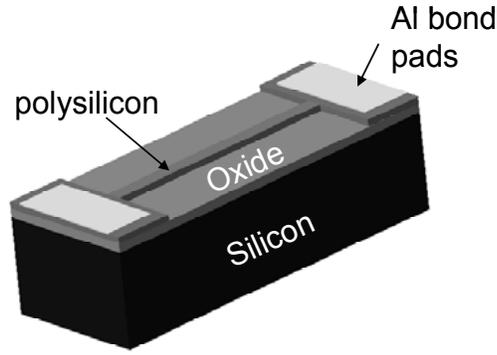
Figure 28 – Schematic of the polysilicon-doped microheater measuring 300 μm long by 10 μm wide.

$$\Omega - \Omega_o = \Delta\Omega_T + \Delta\Omega_\sigma = \left(\frac{\partial\Omega}{\partial T}\right)_\sigma (T - T_o) + \left(\frac{\partial\Omega}{\partial\sigma}\right)_T (\sigma - \sigma_o) \; . \tag{31}$$

If we solve Eq. 31 for $(\sigma - \sigma_o)$, note that $(T - T_o) = (T_\Gamma - T_o)$, and rewrite $\Omega - \Omega_o$ in terms of T_Ω from Eq. 29, a simple expression for the applied stress is obtained in terms of the "linewidth" and "peak" temperatures and the slopes of the calibration curves in Figs. 7 and 27.

$$(\sigma - \sigma_o) = \frac{(\partial\Omega/\partial T)_\sigma}{(\partial\Omega/\partial\sigma)_T} (T_\Omega - T_\Gamma) \tag{32}$$

Eq. 32 is used with measurements of T_Γ and T_Ω to obtain an estimate of the biaxial stress field at the surface of the test sample described next.

7.2 Test Sample Preparation

The test sample consisted of a phosphorous-doped polysilicon beam deposited on a 3.9-μm-thick layer of thermal oxide, which was supported by a 500-μm-thick layer of silicon. The beam was 10 μm wide by 300 μm long and had a thickness of 2.2 μm. The final doping of the microheater was 10^{20} atoms/cm^3 and was achieved using an ion-implantation procedure. A schematic of the structure is shown in Fig. 28. The devices were used without releasing them from the underlying oxide layer in order to constrain the deformation of the beam, which created appreciable levels of thermally induced stress. This sample provided an ideal test bed for demonstration of the simultaneous temperature-stress measurement technique because the profiles of both temperature and stress were essentially constant across the length of the beam.
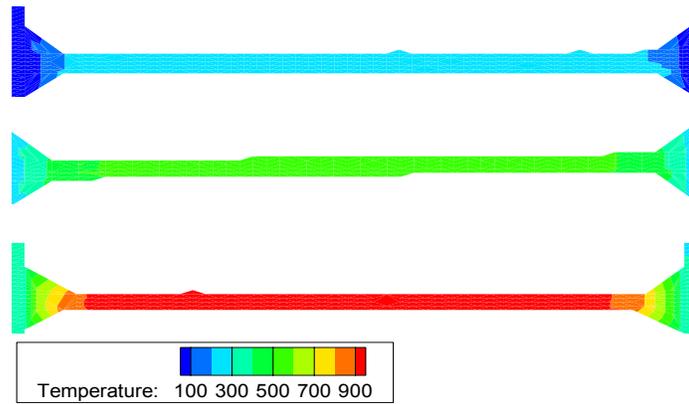
Figure 29 – Linewidth-based temperature (°C) maps of the microheater at 240 mW (Top), 480 mW (middle), and 1000 mW (bottom). Note that the same temperature scale is used for each figure.

Such simple physical profiles provide a known response against which the measured values can be compared, and from which the precision in the measurements can be estimated from the scatter in the experimental data.

7.3 Experiments

Raman spectra were obtained over a 2-D grid of points on the surface of the microheater test specimen. Figure 29 displays the 2-D linewidth-based temperature maps of the microheater as a function of heater input power. All temperatures were based on a single linewidth realization. The temperatures were observed to be uniform throughout the central portion of the microheater at each power level, confirming the expected near-constant physical profiles. Only near the ends of the microheater, where the interconnect pads serve as a thermal sink, is there an appreciable temperature gradient. Since the thermally induced stress distribution should follow the temperature distribution, this mapping procedure indicates that the stress should be constant in the middle of the heater as well.

A comparison between the linewidth- and peak-shift-based temperature profiles of the powered microheater is shown in Fig. 30. One-dimensional profiles of T_Γ and T_Ω have been obtained by averaging the linewidth and peak-shift data over the width of the beam and applying Eqs. 14 and 15. This averaging procedure was performed to reduce measurement noise, particularly in the linewidth-based data. The results show a significant difference between T_Γ and T_Ω, which is of order of 30°C at 240 mW and 60°C at 480 mW of dissipated power. The minimum Raman-detectable stress in Si under isothermal conditions has been reported to be
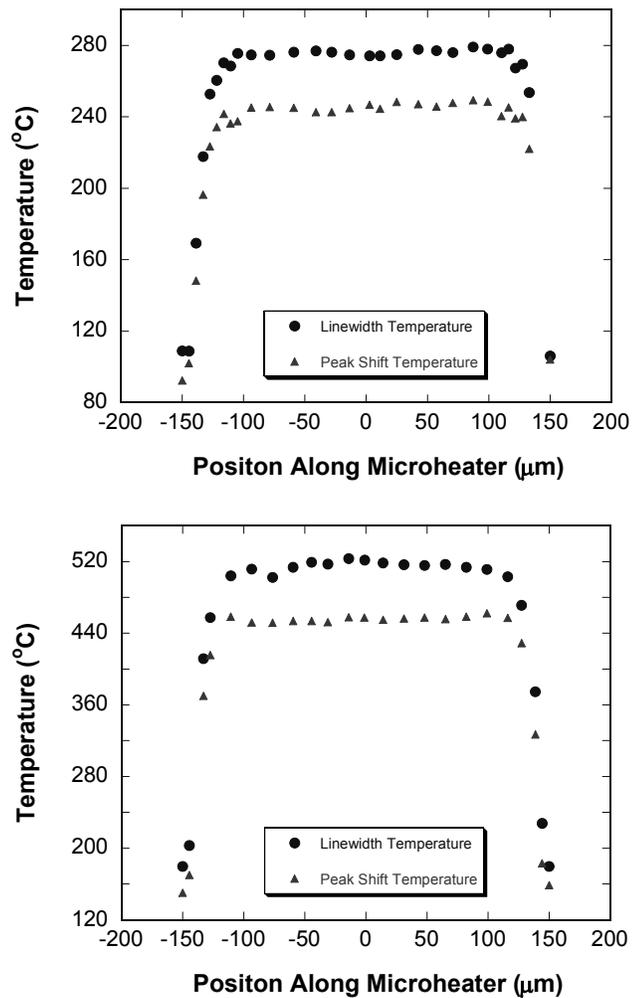
Figure 30 – Temperature distribution across the length of the microheater when dissipating 240 mW (top) and 480 mW of power (bottom). The peak-shift method significantly under predicts the temperature, indicating the expected compressive stress.

±25 MPa [57], which corresponds to a value of $T_\Omega - T_\Gamma$ of ±4.1°C. The discrepancy between temperature measurements in Fig. 30 is much greater than this threshold, indicating that significant stress is present in the device. Furthermore, since $T_\Omega < T_\Gamma$ a compressive stress is present, as would be expected for the heavily constrained thermal expansion experienced by the unreleased test structure.

Since the relative impact of temperature on the Raman peak shift is larger than the impact of stress, noise in the measurement of T_Γ is amplified in the measured stress profiles. To mitigate this effect, the T_Γ data were fit to an analytically based form of the temperature profile. The unreleased beam structure was modeled by considering an energy balance between: (1) 1-D axial conduction, (2) uniform Joule heating, and (3) lateral heat losses that were proportional to the beam surface area and local temperature. With constant thermal conductivity and electrical resistivity, the governing differential equation for this steady-state heat-transfer problem is given by,

$$\frac{d^2\theta}{dx^2} - M^2\theta + Q = 0 \quad , \tag{33}$$

where x is the normalized axial position along the heater, $\theta = T(x) - T_{ref}$, is the difference between the local heater temperature and an appropriate reference temperature, M^2 is a parameter describing the relative importance of lateral heat losses to axial conduction, and Q represents the relative importance of joule heating to axial conduction. The general solution to Eq. 33 is given by,

$$\theta(x) = \frac{Q}{M^2} + K_1 \sinh Mx + K_2 \cosh Mx \quad . \tag{34}$$

The constants K_1 and K_2 and parameters Q and M were varied in four-parameter fits to Raman temperature data obtained from the constrained test sample of Fig. 28 as well as two different V-shaped thermal actuator designs. As shown in Fig. 31, Eq. 34 was found to fit the data from all 3 MEMS test samples extremely well, and this expression can be viewed as a physically based temperature filtering function for electrically heated MEMS structures with 1-D axial conduction.

The filtered linewidth-based temperature data were used with their corresponding Stokes-peak-based temperatures and Eq. 32 to obtain an estimate of the 1-D profile of biaxial stress on the constrained test specimen for dissipated powers of 240 and 480 mW. The stress data are
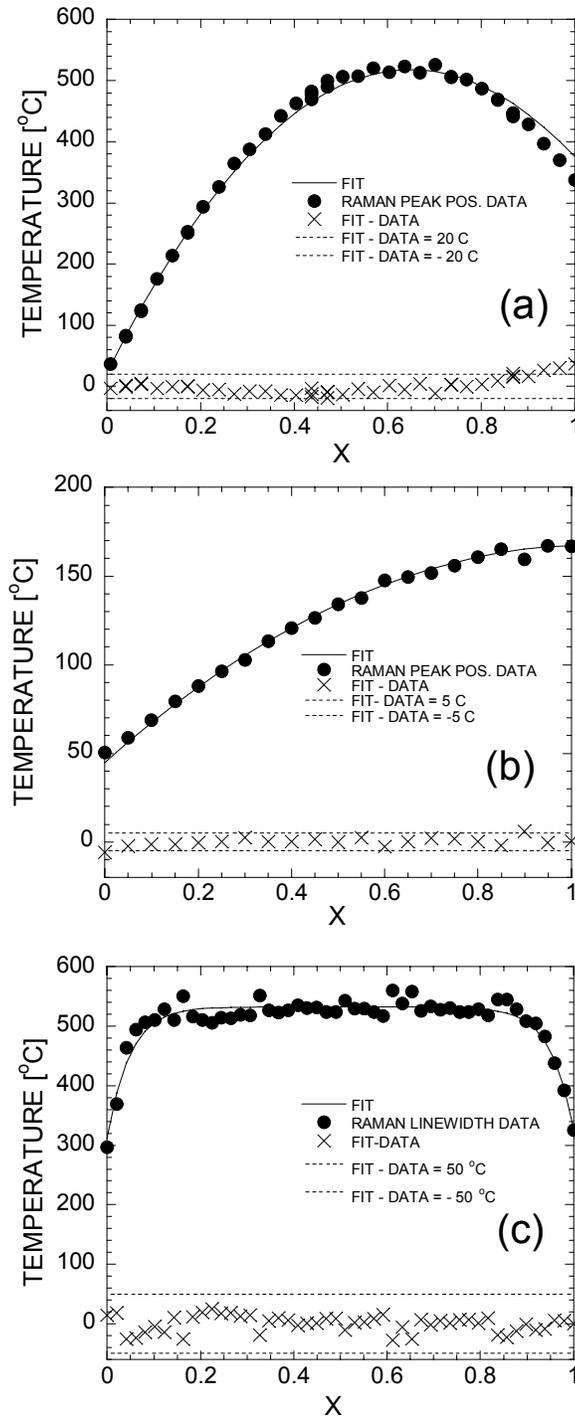
Figure 31 – Fits of the form of Eq. 34 to Raman-measured temperature data for (a) a SUMMiT-V-fabricated, V-shaped thermal actuator [4], (b) a NIST-supplied bulk-crystal silicon V-shaped thermal actuator [58], and (c) the constrained polysilicon beam shown in Fig. 28. The function fits all three sets of data and captures both the "top hat" behavior seen in (c) and the "asymmetric parabola" profiles in (a) and (b), depending upon the magnitudes of the physical parameters M and Q in Eq. 34. The difference between the fit and the Raman temperature data is shown by $\times$ symbols on the plots, with the bounds on this difference indicated in the plot legend shown as dashed lines.

presented in Fig. 32, where we can see that the measured stress is near-constant across the center portion of the beam. The results are compared to mechanical finite-element-analysis (FEA) simulations of the constrained beam, with the measured linewidth-based temperature profile used as an input. At 240 mW, the average Raman-measured stress over the center portion of the beam was -153 MPa, compared to -160 MPa from the FEA simulations, a difference of 4.3%. Average biaxial stress values of -304 MPa and -348 MPa were obtained for the Raman- and FEA-based results, respectively, at 480 mW of dissipated power, a difference of 12.6 %. An initial estimate of the precision in the Raman stress measurements could be obtained from the scatter in the data over the constant-stress portion of the test structure. From this, we estimate the precision in the Raman stress measurement to be ~ ±40 MPa with an uncertainty in the simultaneously measured linewidth-based temperature of ± 15 K[‡].

7.4 Simultaneous Temperature-Stress Mapping Conclusions

Micro-Raman spectroscopy is used to simultaneously obtain temperature and stress profiles along the length of a functioning polysilicon microheater. Comparison of the measurements to finite-element calculations shows that the method holds promise for applications in active devices where combined thermomechanical processes are of importance. While linewidth-based measurements of temperature are typically not as precise as Stokes-peak-based data, linewidth-based thermometry is shown to be feasible by averaging multiple realizations and/or by fitting an appropriate functional form to the data. The method provides one of the only experimental techniques which can nondestructively monitor stress and temperature in working MEMS devices. Future efforts should emphasize the impact of the general state of stress and the temperature dependence of the Raman stress calibration, which was performed only at room temperature.

[‡] As determined from the scatter in linewidth-based temperatures measured on flexure-style actuators presented in Section 5.2
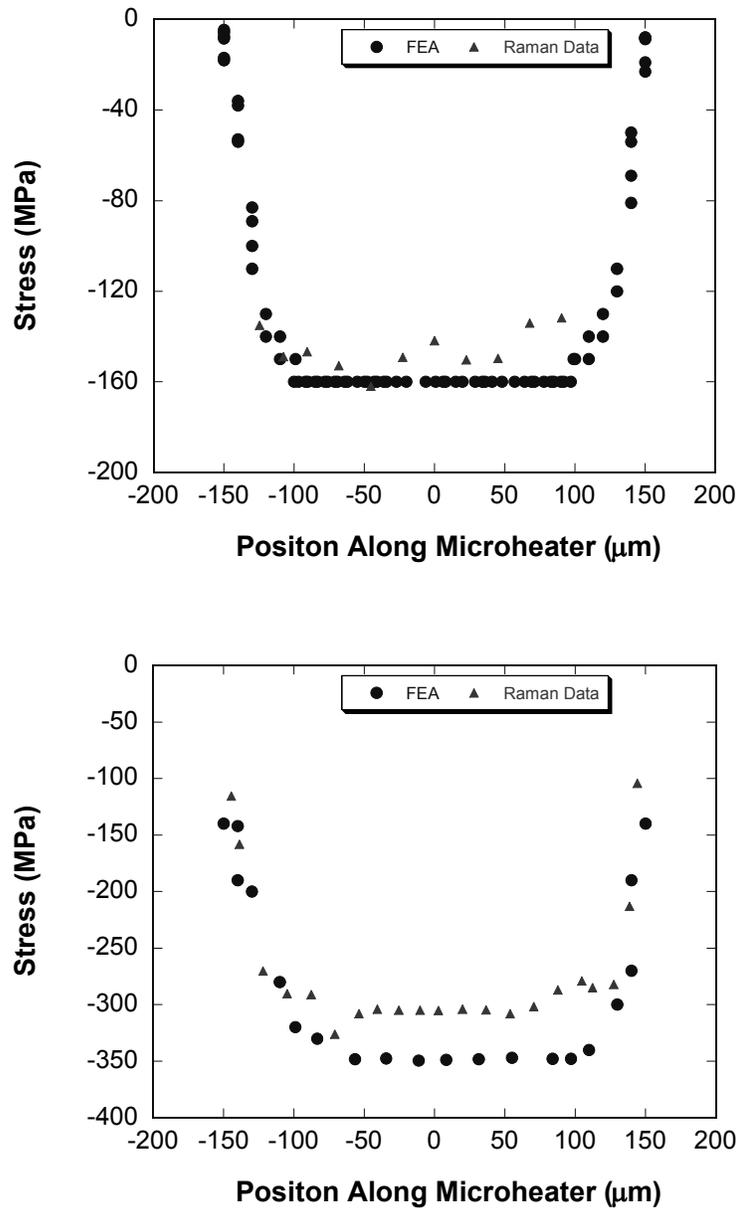
Figure 32 – Data comparison of biaxial stress, calculated using finite-element analysis (FEA) and measured with Raman spectroscopy, for power dissipation levels of 240 mW (top) and 480 mW (bottom).

8. MEMS THERMOMETERY BY SURFACE THERMOREFLECTANCE

8.1 Principles and Technical Background

Changes in temperature can affect a material in different ways, one of which is a change in the value of the complex index of refraction. Because surface reflectivity is directly linked to the fundamental optical properties of the material, knowledge of the relationship between surface reflectivity and temperature can be exploited for temperature diagnostics. This premise forms the basis for the thermoreflectance thermometry technique.

Many mechanisms can contribute to the change in reflectivity as a function of temperature [20, 59], including changes in electron energy bands, increased transitions near the Fermi level at higher temperatures, and increased phonon-electron interactions at high temperatures, among others. In some materials, especially in metals and some semiconductors, the resulting change in optical reflectivity is linear with temperature. The sensitivity of this change with temperature is quantified by the thermoreflectance coefficient, κ, which relates the change in reflectivity per unit change in temperature. Typically, κ is of order of 10^{-4}–10^{-6} K^{-1} and depends on the wavelength that is used to probe the surface [20-23].

In addition to being an optical non-invasive technique, thermoreflectance has the potential for providing micron-scale spatial resolution and sub-nanosecond temporal resolution [6, 24-27]. While spatial resolution is limited by the diffraction limit of the optics involved in the detection scheme, the theoretical limit of the temporal resolution is determined by the order of the processes involved in the reflectance, which can be on the order of picoseconds in metals [20]. The drawbacks to this technique are the challenging calibration of the thermoreflectance coefficient and possible shifts in calibration arising from deflection/deformation of the device during its operation.

8.2 Experimental Setup

To carry out the temperature and reflectivity measurement, we use the experimental setup shown schematically in Fig. 33. The laser source is a frequency-stabilized HeNe laser (λ = 632.8 nm) with a linearly polarized output at 1 mW. The active stabilization in this laser makes it ideal for thermoreflectance measurement because it reduces any noise that might be introduced by the fluctuations in the beam power. The power output of the laser is modulated by a mechanical chopper at frequencies between 500 Hz and 1000 Hz. The beam is sampled by a 90/10 plate beam splitter and a large-area photodiode to serve as a reference signal that accounts
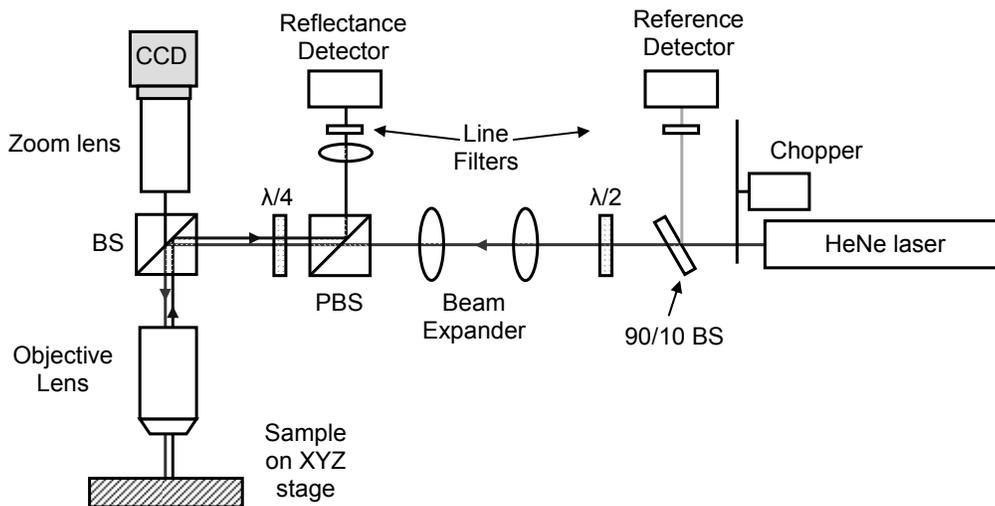
Figure 33 – Experimental setup for thermoreflectance measurements.

for fluctuations in the laser intensity. A beam expander is used to sufficiently to fill the entrance aperture of the objective lens and ensure the smallest focused spot size possible (maximum spatial resolution). A $\lambda/2$ waveplate in combination with a polarizing cube beam splitter (PBS) is used to attenuate the laser intensity and prevent back reflections towards the laser cavity. The beam transmitted by the PBS has its polarization rotated by a $\lambda/4$ waveplate to a circular polarization state. The circularly polarized light incident on the sample is reflected with the polarization rotation sense reversed and is transmitted through the $\lambda/4$ plate once again, such that the reflected signal-beam polarization is orthogonal to the incident probe beam. The signal is rejected by the PBS and onto a second large-area photodiode for detection.

Both large-area detectors (NewFocus Model 2031) are equipped with a laser-line interference filter that transmits only the 632.8-nm laser wavelength and blocks stray illumination from the detectors. A 75-mm focal-length convex lens is used to focus the collimated reflectance signal onto each detector. The signals from each detector are lock-in amplified, using the chopper sync signal as the frequency reference for the lock-ins. By tracking the reference beam in conjunction with the thermoreflectance signal, we can compensate for small fluctuations in the stabilized laser power.

The sample surface is imaged through a Navitar Zoom lens and a CCD camera. A 20× Mitutoyo (f = 10 mm) objective aids in both the focusing of the probe beam and in imaging of the sample surface. With the expanded beam filling the entrance aperture of the objective, this objective lens allows for a diffraction-limited spot size of ~ 600 nm. The actual spot size obtained is approximately 750 nm in diameter, as seen in Fig. 34.

1 μm
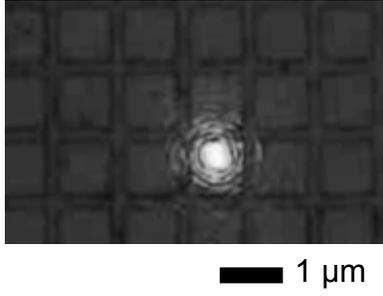
Figure 34 – Laser spot size imaged onto a 1-μm × 1-μm grid. The spot size is ~ 0.75 μm in diameter.

8.3 Thermoreflectance Data Interpretation

Thermoreflectance relies on the change in the surface reflectivity of a solid-state sample with temperature. For most metals and some semiconductors, this change is linear with temperature over some temperature range at some specific wavelength. The mathematical relationship describing this phenomenon is given by

$$\frac{\Delta R}{R_o} = \kappa(T - T_o) \quad , \tag{35}$$

where R is the surface reflectivity, expressed as,

$$R(T) = R_o + \frac{dR}{dT}(T - T_o), \tag{36}$$

where R_o is the surface reflectivity at temperature T_o, and the constant $\kappa = 1/R_o \times dR/dT$ is the thermoreflectance coefficient of the sample. With a valid value of κ, the temperature change $\Delta T = (T - T_o)$ experienced by the surface can determined through the measurement of the reflectivity change, $\Delta R / R_o$.

While values for the thermoreflectance coefficients can be found in the literature, accurate temperature measurements require calibration of κ on the material to be probed because slight differences in the surface quality and preparation can impact the value [20, 21, 24, 60]. Calibration of the thermoreflectance coefficient is typically carried out by heating the sample to be measured (or an identical substitute) to known temperatures and measuring the change in surface reflectivity. If the reflectivity is linear with temperature, Eq. 35 applies and the thermoreflectance coefficient is given by the slope of a plot of $\Delta R / R_o$ versus temperature.

With the optical system shown in Fig. 33, the signal from each photodiode (reference and reflectance signal) is read by a lock-in amplifier, using the chopper's modulation frequency as

66

the reference for lock-in amplification. Both detectors have built-in gain resistors and generate a voltage that is proportional to the laser power incident on the detector. At the reflectance detector, the measured voltage is proportional to the laser power reflected from the sample,

$$V_S = c_1 R_S P_L \quad , \tag{37}$$

where c_1 is a proportionality constant, R_S is the sample reflectivity, and P_L is the laser power. Likewise, the reference voltage is proportional to the laser power,

$$V_R = c_2 P_L \quad , \tag{38}$$

where c_2 is a proportionality constant. While using the reflectance signal, V_S , alone can potentially permit the measurement of the temperature-induced reflectivity change, small fluctuations in the laser power can introduce the noise and uncertainty in the measurement. By monitoring the laser power in real-time during the measurement, fluctuations in the laser power can be accounted for and low-frequency noise in the measurement can be reduced.

8.4 Calibration

The thermoreflectance calibration is performed by placing the sample in a temperature-controlled heating stage (Linkam TS-1500) and recording the change in reflectivity for a range of known temperatures. At the start of the calibration process, with the sample in equilibrium at an initial temperature, the reflectivity and reference signals are captured. The data are analyzed through regression analysis to obtain the factor G that, when multiplied by the reference signal, V_R, nullifies the difference between the reference and reflectance voltage signals at the initial temperature, i.e.:

$$V_R' = V_R G = V_S(T_o) = V_o \tag{39a}$$

$$\Delta V = V_o - V_R' \approx 0 \tag{39b}$$

In this manner, the modified reference signal, V_R', is a direct indicator of the reflectance at the temperature T_o.

During the calibration process both V_R' and V_S are determined at every temperature step. The relative change in the voltage, $\Delta V/V_o$, is then equal to the relative change in reflectivity, $\Delta R/R_o$:

$$\begin{aligned}
\frac{\Delta V(T)}{V_o} &= \frac{V_S(T) - V_R{}'}{V_S(T_o)} \\
&= \frac{V_S(T) - V_S(T_o)}{V_S(T_o)} \\
&= \frac{c_1 P_L R(T) - c_1 P_L R(T_o)}{c_1 P_L R(T_o)} \\
&= \frac{R(T) - R(T_o)}{R(T_o)} \\
\frac{\Delta V(T)}{V_o} &= \frac{\Delta R(T)}{R_o}
\end{aligned} \tag{40}$$

If the reflectivity is linear with temperature (see Eq. 35), then

$$\frac{\Delta V(T)}{V_o} = \frac{1}{R_o}\frac{dR}{dT}(T - T_o) = \kappa(T - T_o), \tag{41}$$

and a plot of $\Delta V/V_o$ as a function of temperature yields a straight line with slope κ, the thermoreflectance coefficient.

While this technique has the advantage of nullifying any dependence on the measurement system (through normalization), it has a drawback in that the signal of interest, namely ΔV, can remain small (assuming an initial voltage of $V_o = 1$ V with $\kappa \sim 10^{-4}$ K^{-1}, $\Delta V \sim 1$ mV for a 10-K temperature change). Since a lock-in detection scheme is used, the most significant source of noise is low-frequency drift resulting from slow fluctuations in the room temperature, laser power, and detector response.

Although an alternative detection scheme can be implemented, which uses a single lock-in to amplify the signal change, ΔV [61], the lack of normalization does not remove any dependence on the irradiation schemes used in the calibration and the temperature-measurement steps. While this single-lock-in technique allows us to obtain a calibration curve, without ensuring identical irradiation conditions during the measurement, the calibration will not be valid during the temperature measurement.

8.5 Noise and Uncertainty

With either technique described above, two distinct types of noise have been identified. The first is a high-frequency, small-amplitude noise that is captured with the data. This type of noise is bit-noise and is the result of quantization of the analog voltage signals by the A/D conversion

of the data-acquisition system. Our data-acquisition system has 12 bits of resolution and a ±1 V input (National Instruments DAQCard-6062E), giving an ultimate measurement resolution of 488 μV. A 1- or 2-bit noise in the data acquisition can result in a deviation of up to ~1 mV, or ~ ±10 K of uncertainty. The impact of this noise is minimized through averaging of the measured signals over time (typically several seconds) at an acquisition rate of 2000 samples/s. The bit-noise uncertainty is thus minimized to better than ±1 K.

The second type of noise is a low-frequency (<1 Hz) drift in the measured signals. The source of the noise appears to lie in the stabilization mode of the HeNe laser, which can operate in a frequency stabilized mode and an intensity stabilized mode. In frequency stabilized operation, the laser power can suffer slow fluctuations in the power of up to 1% of the full power during the course of operation. Such fluctuations would correspond to a drift in the signal of >2 mV/hr corresponding to an uncertainty of up to ~ ±10 K, depending on the thermoreflectance coefficient. Operating the laser in the intensity stabilized mode, however, reduces the power fluctuations by a factor of 5–10, reducing the uncertainty to better than ±2 K. The potential problem of low-frequency drift can appear most significantly during the calibration procedure, where measurements are taken over prolonged periods of time (typically 30 minutes to 1 hour), without the capability to apply a correction for the drift. For measurements on devices that can be powered on and off, drift in the system can be corrected for by obtaining measurements in the unpowered and powered conditions.

The final contribution to the measurement uncertainty comes from the uncertainty in determining the thermoreflectance coefficient for the device or system under study. While the reflectivity of many materials can be described by Eq. 35, the temperature range over which the equation is valid can impact the linearity of the reflectance response [60], and, therefore, the uncertainty in the determination of the thermoreflectance coefficient.

8.6 Calibration Results

8.6.1 Silicon (100)

The reflectivity of single-crystal silicon as a function of temperature has been studied extensively in the literature [60, 62-64] and thus provides for an ideal system to evaluate the
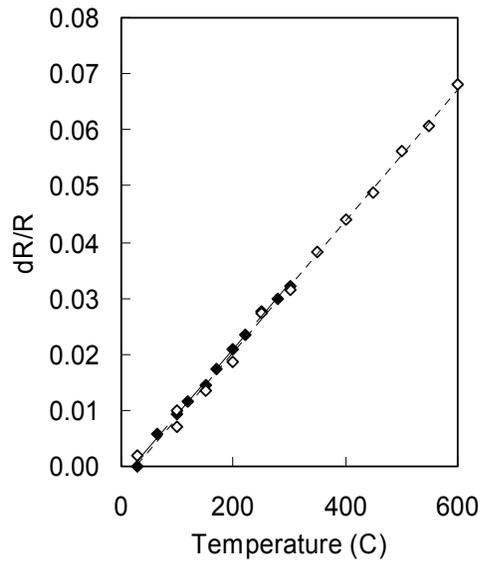
Figure 35 – Thermoreflectance response of a single-crystal silicon (100) surface for HeNe-laser irradiation at λ = 632.8 nm. The closed and open symbols represent two datasets measured approximately one year apart. The extracted thermoreflectance coefficient from the data is κ = $(1.176 \pm 0.0188) \times 10^{-4}$ K^{-1}.

operation of the thermoreflectance setup. For silicon, the surface reflectivity increases linearly with temperature at all wavelengths between 400–1100 nm [60, 62-64]. Our calibration of Si was carried out by placing a single-crystal silicon sample, with the 100 face normal to the incident laser beam, in a temperature-controlled heating stage. The sample was heated from 30°C to 600°C in 50°C increments and the reflectance and reference signals were captured at each step. At each temperature step, the sample is allowed to equilibrate for two minutes before taking the measurement.

The thermoreflectance response for silicon is shown in Fig. 35. Over the temperature range explored, the thermoreflectance signal is linear as expected, and results in a thermoreflectance coefficient of κ = $(1.176 \pm 0.0188) \times 10^{-4}$ K^{-1}. This value compares well with values found in the literature of between 1.118×10^{-4} K^{-1} [62] and 1.204×10^{-4} K^{-1} [64]. The uncertainty in the calibration contributes to a temperature uncertainty of $\pm$ 1.5°C at 100°C and $\pm$9.5°C at 600°C. Considering the other contributions to the uncertainty introduced by the detection system and the laser power fluctuations, the total measurement uncertainty is estimated to be $\pm$2.7°C at 100°C and $\pm$9.75°C at 600°C, calculated by vector summing the component-level uncertainty contributions [55].
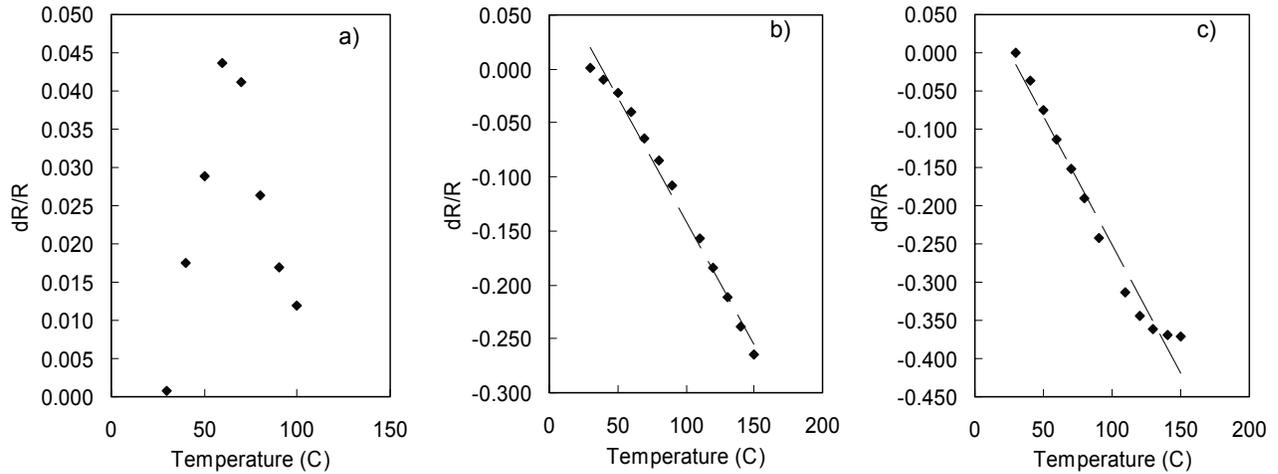
Figure 36 – Thermoreflectance responses for various SUMMiT-V polysilicon layers for HeNe-laser irradiation at $\lambda = 632.8$ nm: (a) Poly1-Poly2 laminate, (b) Poly3, and (c) Poly4.

8.6.2 SUMMiT Polycrystalline Silicon

Although polycrystalline silicon (polysilicon) can have optical properties very similar to bulk silicon, slight differences in the growth method, material thickness, doping concentration, etc. can impact the thermoreflectance response [60]. Unlike the bulk-silicon samples which produced consistent and reproducible thermoreflectance responses, calibration of polysilicon layers generated varying thermoreflectance responses, which were linear over a narrow temperature range, but behaved non-linearly outside this range, as shown in Fig. 36.

Since the tested polysilicon films are on the order of 2.25 μm in thickness, the thermoreflectance response is affected by thin-film interference effects arising from multiple reflections from the top and bottom surface of the film [65]. The interference phenomena are the likely explanation for the relatively large thermoreflectance coefficient of 2–4 $\times$ 10^{-3} K^{-1} observed in the linear portions of the responses for Poly3 and Poly4. The nonlinearity introduced by interference is most evident in the laminated Poly1-Poly2 structure, which has the interface between the two layers in addition to the front and back surfaces. The nonlinear responses of the SUMMiT polycrystalline silicon films complicates the temperature measurement for devices and structures made up of these layers.

8.6.3 SUMMiT Al-Cu

The metallization layer in the SUMMiT-V processing is an aluminum-copper alloy. Ideally, thermoreflectance would be a very useful tool for thermometry of metal-coated surfaces, which cannot be probed with Raman microscopy techniques. However, metal films have the
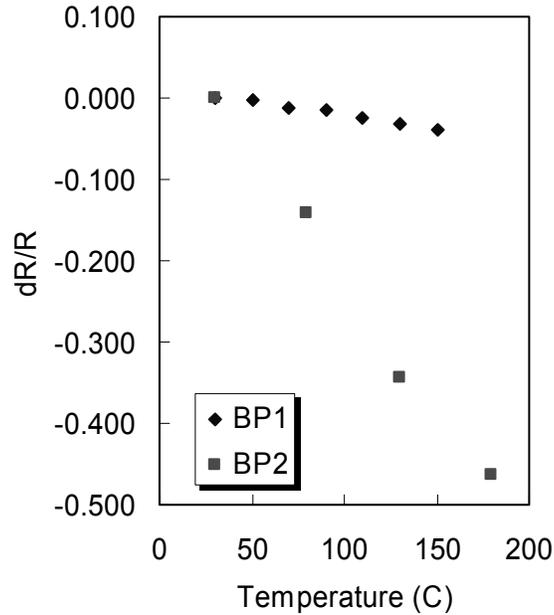
Figure 37 – Thermoreflectance response of two separate metallized bond pads coated with SUMMiT Al-Cu metallization for HeNe-laser irradiation at $\lambda = 632.8$ nm.

disadvantage of suffering irreversible changes during prolonged heating, due to oxidation, adhesion-layer segregation, and dewetting, which can hinder the calibration step.

To avoid any irreversible metallization problems, the calibration of a SUMMiT-V metallized bond pad was carried out in the temperature range from 30°C to 150°C. Over this narrow range, the measured thermoreflectance coefficient was $\kappa = -(3.33 \pm 0.15) \times 10^{-4}\,\mathrm{K}^{-1}$. The temperature-measurement uncertainty associated with the reliability of this thermoreflectance coefficient is approximately ±8°C. While this thermoreflectance response is linear and conforms to Eq. 35, the response is very hard to reproduce and is strongly dependant on surface quality. Indeed, repeating the measurement on other parts coated with the same metallization produced drastically different response, as shown in Fig. 37.

8.7 Device Measurements

To evaluate the effectiveness of the thermoreflectance technique for thermometry in a real device, we measured the temperature of a bulk-micromachined, silicon-on-insulator (SOI), V-shaped electro-thermal actuator. The actuator had 600-μm-long legs that were 10 μm thick and 10 μm wide and connected to a 30-μm-wide central shuttle, as shown in Fig. 38. The device was developed by the Intelligent Systems Division at the National Institute of Standards and Technology (NIST) [58]. Being an electrically-powered device, it presents the possibility of obtaining measurements with the device powered and unpowered to properly correct for any drift present in the thermoreflectance measurement system.
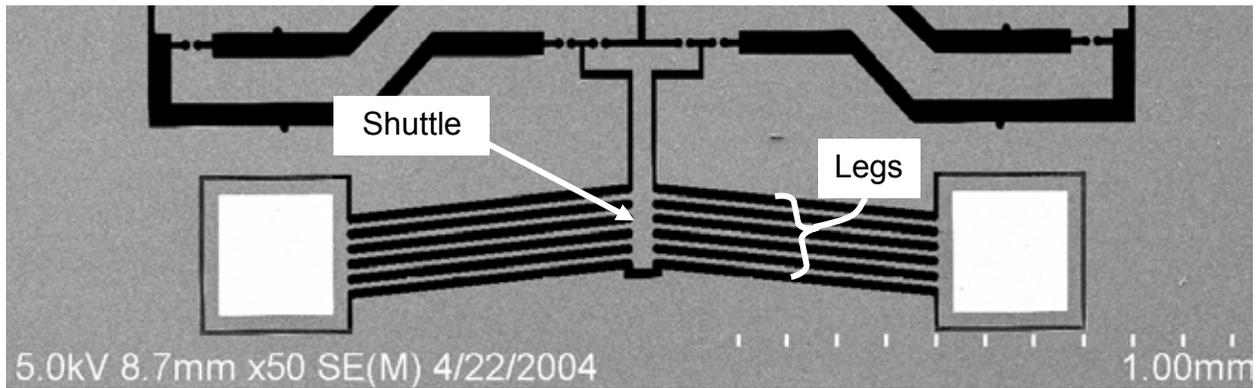
Figure 38 – SEM image of a typical NIST-fabricated electro-thermal actuator. The actuator legs are 600 μm long × 10 μm wide × 10 μm thick. The shuttle is 30 μm wide × 10 μm thick (From Ref. [58]).

The temperature at the center of the shuttle was measured for increasing applied voltage to the device. Using the calibrated thermoreflectance coefficient for single-crystal silicon (κ = [1.176 ± 0.0188] × 10^{-4} K^{-1}) we measure a quadratic temperature dependence with voltage, with a maximum temperature of ~150°C at 10 V. Since the devices are Joule heated, the quadratic behavior is expected. Moreover, because the device is fabricated from silicon, the temperature can be corroborated by repeating the measurement with Raman microscopy. As seen in Fig. 39a, there is good agreement between the two measurements. The differences between the two measurements can be explained by taking into account the initial "cold" temperature of the device. The room temperature of the device when measured with Raman was ~ 28°C, while the temperature was ~22°C for the thermoreflectance measurements, as determined with a thermocouple placed next to the device. This difference in initial temperature correctly accounts for the offset between the two measurement techniques, as demonstrated by a plot of the change in temperature during operation, which is shown in Fig. 39b.

8.8 Thermoreflectance Conclusions

Thermoreflectance is a technique that can provide temperature measurements at micron-scale spatial resolution, with a potential for sub-microsecond temporal response. The effectiveness of the technique depends strongly on the ability to properly calibrate the thermoreflectance coefficient of the surface to be probed. With our instrument, we can correctly
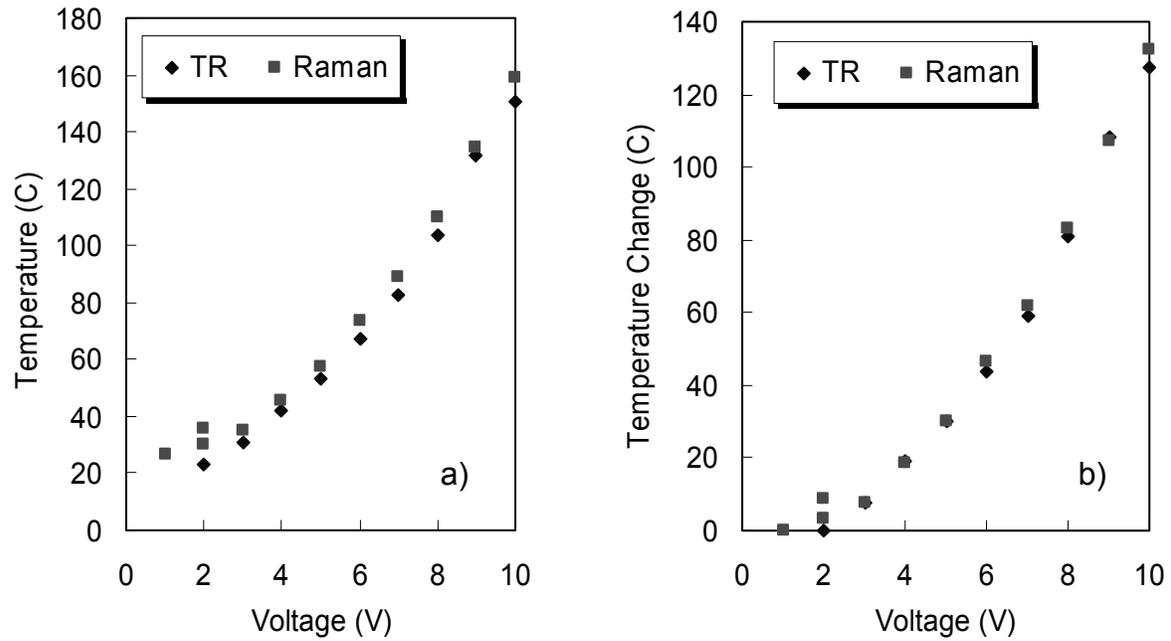
Figure 39 – (a) Temperature of the center shuttle of an ET bent-beam actuator as a function of operating voltage, measured with thermoreflectance (TR) and Raman thermometry techniques. Initial device temperatures for both measurements were 22°C for thermoreflectance and 28°C for Raman. (b) Relative temperature change in shuttle temperature measured with both techniques.

measure the thermoreflectance response of bulk crystalline silicon in comparison with values published in the literature. For bulk crystalline silicon, the uncertainty in the temperature measurement is estimated to be ±2.7°C at 100°C and ±9.75°C at 600°C.

For other surfaces of interest in this study: SUMMiT-V polycrystalline silicon and metal layers, the thermoreflectance response was nonlinear, which complicates thermometry of these surfaces. In the case of devices fabricated out of polycrystalline silicon films, differences in film deposition conditions affect the optical properties sufficiently to produce a nonlinear thermoreflectance response. In addition, the relatively small thicknesses of the layers introduce contributions from thin-film interference that impact the sample's reflectivity. Metal layers, while exhibiting a linear reflectance response, did not produce consistent results across different samples.

Thermoreflectance was used to measure the temperature of a single-crystal silicon-on-insulator, bulk-micromachined, electro-thermal actuator. Using the calibrated thermoreflectance coefficient for single-crystal silicon, the quadratic temperature dependence of the center shuttle for increasing operating voltages is correctly measured with this technique. Moreover, the thermoreflectance-measured temperature increases are in good agreement with data obtained by Raman microscopy.

9. LDRD PROJECT SUMMARY AND DIRECTIONS FOR FUTURE WORK

9.1 Project Summary

An LDRD-funded effort has been undertaken for the purpose of developing noninvasive and noncontact thermometry diagnostics for working MEMS devices. Two laser-based diagnostic techniques were cultivated: (1) Raman spectroscopy and (2) thermoreflectance, with Raman emerging as the primary diagnostic of choice and thermoreflectance assuming a complimentary role. Both methods readily provide an in-plane spatial resolution of ~1 μm, which is sufficient for resolving the fine-scale features of most working microsystems. The methods are nonperturbing in nature, and require only optical access to the MEMS surface to be probed, with no special modifications to MEMS device design.

Raman spectroscopy was demonstrated to be an effective tool for temperature mapping on MEMS under steady-state conditions. As part of this effort, an understanding of the physics behind the temperature dependence of solid-state Raman spectra was obtained, as summarized in this report. The temperature dependence of the Stokes-shifted Raman peak position (phonon frequency), the width of the Raman lines (phonon lifetime) and the relative intensities of the Stokes- and anti-Stokes-shifted Raman peaks (phonon thermal occupation) were all evaluated as temperature indicators. In applications without significant stress gradients in the MEMS material, the Stokes peak position was found to be the most robust indicator of temperature. When applied stress was a factor, a linewidth-based temperature metric was used to eliminate stress-induced bias in the results. Uncertainties in Raman-measured temperatures ranged from ±10 K for peak-shift-based temperature estimates, to ±15 K in the linewidth-based temperatures for MEMS applications on Si. The Raman diagnostic cultivated here was applied for practical thermometry of poly- and single-crystal silicon electro-thermal actuators, GaN-fabricated transistors, and polysilicon microheaters. In applications with both significant heating and applied stress, we have demonstrated the potential of the Raman technique for simultaneous mapping of both temperature and stress.

Thermoreflectance was demonstrated as a complement to Raman, as the reflectance-based diagnostic may have utility for highly transient measurements and for measurements on metallic or Raman-inactive materials, where conventional Raman spectroscopy is not possible. The temperature dependence of the thermoreflectance response was calibrated on bulk silicon, SUMMiT-V-fabricated polysilicon and SUMMiT-V-fabricated Al-Cu metallized surfaces. Thermoreflectance thermometry experiments were conducted on a working bulk-Si-fabricated electro-thermal actuator, and the reflectance-based temperatures were found to be in good

agreement with Raman-derived results. Thermoreflectance calibrations for SUMMiT-V polysilicon layers and Al-Cu metallized layers displayed a nonlinear temperature dependence, which increases the complexity of reflectance-based thermometry for these materials.

9.2 Directions for Future Work

Our current Raman and thermoreflectance diagnostics are limited to steady-state conditions with a diffraction-limited spatial scale of ~ 1 μm. In addition, the time required to obtain a single Raman-derived temperature profile can be as much as 3-4 hours. Future efforts in the arena of MEMS thermometry should be directed at the following overarching goals.

1. Reducing the data-acquisition time for steady-state profiling measurements
2. Improved temporal resolution – transient MEMS thermometry
3. Improved spatial resolution – submicron and nanoscale systems

The push toward submicron and even nanoscale systems at Sandia will amplify the need for extreme-resolution thermal diagnostics. Transient thermal processes in microscale, silicon-based systems typically occur on the order of milliseconds, such that a temporal resolution of order 10 to 100 μs is required to resolve these events. Adding such a transient capability will provide an improved understanding of problems in thermal cycling of repetitively driven MEMS [4] and thermal damage in optically initiated microsystems [66, 67].

Improvements to our existing thermoreflectance capability may quickly address the need for transient thermometry, at least on a qualitative or relative basis. We have also identified four Raman-variant diagnostics for future development, which are briefly summarized in the following subsections.

9.2.1 Near-Field Raman Scattering (NFRS)

With NFRS, the spatial resolution of Raman thermometry is improved by a reduction in the effective probe-laser spot size. Conventional Raman microscopy systems, such as the Sandia instrument shown in Fig. 4, focus the probe laser beam at the sample using a microscope objective placed in the far field. Far-field optical systems are diffraction limited to a focused spot diameter of $d = \lambda/2\,\mathrm{NA}$, where λ is the laser wavelength and $\mathrm{NA} = n \sin \theta$ is the numerical aperture of the focusing objective based on the index, n, at the focal point. For visible laser beams focused onto silicon samples, spot sizes are typically limited to ~ 1 μm. This limit can be reduced by imaging Raman-scattered light through a near-field aperture which is smaller than the

76

diffraction limit and placed very close to the sample. Probe-laser coupling and backscattered Raman collection through such a small aperture is enhanced if the aperture is fabricated as a high-index solid-immersion lens. This arrangement has been exploited by Fletcher *et al.* [7] who used a microfabricated silicon lens in contact with the sample to demonstrate infrared thermal imaging with a resolution of $\lambda/5$. A similar near-field solid-immersion microscope could be used to improve the resolution of our Raman instrument to a few 100s of nm.

9.2.2 Coherent anti-Stokes Raman Scattering (CARS)

CARS probing of solid-state materials may improve the temporal resolution of MEMS thermometry via a significant enhancement in Raman signal levels, which results in reduced data-integration time for a given signal-to-noise requirement. With CARS, an enhanced-strength and spatially coherent (laser-like) Raman signal is generated through the nonlinear third-order susceptibility of the probed medium. The frequency difference between overlapping pump and Stokes-shifted laser beams is tuned to a Raman resonance to drive a polarization at $\Omega = \omega_p - \omega_s$, where ω_p and ω_s are the pump- and Stokes-laser frequencies, respectively. A second pump photon is scattered from the induced polarization, resulting in an anti-Stokes-shifted CARS photon at frequency $\omega_{as} = 2\omega_p - \omega_s$. In addition to signal enhancements of several orders of magnitude, the coherent laser-like nature of the CARS signal beam permits near-100% signal collection. CARS spectra are similar to spontaneous Raman spectra, and CARS has been demonstrated in forward scattering [68], as well as backscattered geometries in Si and other solid-state materials [69, 70]. To our knowledge, CARS has never been exploited for solid-state thermometry, but has been extensively used for gas-phase temperature measurements at Sandia and elsewhere [28, 71-73].

The main technical challenges associated with transient CARS thermometry in the solid-state lie in the complexity of the experimental setup and the high peak laser powers required to drive the nonlinear optical process, which may damage or artificially heat MEMS devices [66, 67]. One potential solution is the use of ultrafast, picosecond-duration pulsed laser systems, which can generate high peak intensities with very modest overall energy deposition. Use of ultrafast sources has the additional benefit of limiting the time resolution to the very short duration of the laser pulse.
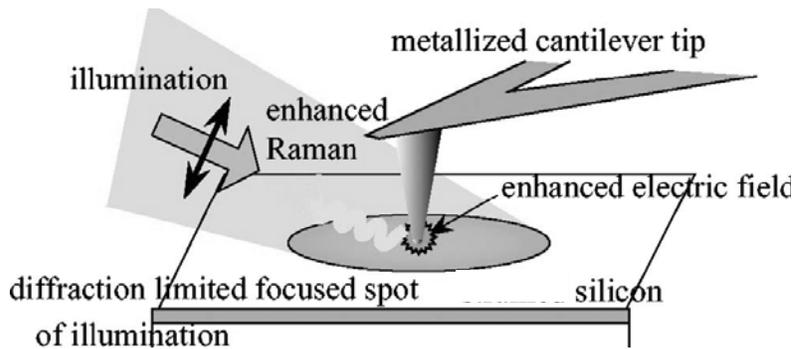
Figure 40 – Surface-Enhanced Raman Scattering (SERS) configuration as illustrated by Hayazawa *et al.* [74].

9.2.3 Surface-Enhanced Raman Scattering (SERS)

The SERS effect has potential to provide both increased spatial *and* temporal resolution Raman-based thermometry. An excellent review of SERS is presented by Campion and Kambhampati [75]. Raman signal enhancements of many orders of magnitude have been observed when a metallized surface of ~10- to 100-nm curvature is placed in close proximity to a probe-laser spot. An electromagnetic enhancement arises when the probe laser beam collectively excites the electron plasma within the sharply curved metallic surface. This collective excitation is termed a plasmon wave and this laser-driven plasmon dramatically enhances the strength of the Raman-scattered electric field. We propose to exploit electromagnetic SERS with the experimental configuration shown in Fig. 40 [74], where a 10-100 nm radius silver-coated atomic-force microscope (AFM) tip is brought into contact with a silicon surface. The probe tip is flood illuminated by the much larger 1-micron laser spot, which drives a plasmon resonance only in the vicinity of the tip. An enhanced Raman signal from the tip region only would result in an extreme spatial resolution on the order of a few 10s of nm. Shortened data acquisition times and potentially transient measurements may also result if the magnitude of the SERS signal is sufficient to deliver adequate Raman signal-to-noise in a microsecond-scale timeframe. As part of this LDRD project, we have obtained metal-coated AFM tips, and constructed a feedback-based nanopositioning system in an attempt to acquire SERS-enhanced Raman spectra. At this juncture no SERS enhancement has been observed, but improvements to our experiment may soon result in SERS detection.

9.2.4 Spectrally Filtered Raman Scattering (SFRS)

The SFRS method aims to improve the temporal resolution of Raman thermometry by removing the need for spectrally resolved detection using a long-read-time CCD camera. The SFRS concept is similar to the filtered-Rayleigh-scattering diagnostic used for gas-phase velocity and temperature imaging at Sandia [76, 77]. The CCD camera in the Raman microscope facility shown in Fig. 4 is replaced by the optical system shown in Fig. 41a. The Raman signal dispersed by the diffraction grating is split into 'filtered' and 'reference' legs. Total Raman intensity is sensed by a photon-counting photomultiplier tube in the reference leg, while a slit oriented normal to the grating dispersion is used to pass only a fraction of the Raman-scattered spectrum to a second photomultiplier. In this manner, the spectral resolution is provided only by a single exit slit, and the need to read multiple spectral elements with a slow-reading CCD camera is replaced by two faster-reading single-element detectors. The temperature sensitivity of the SFRS technique is illustrated in Fig. 41b, where the temperature-induced shift and broadening of the Si Raman peak changes the fraction of the Raman signal that is passed, or 'filtered', by the exit slit. When the spectral location and bandpass of the exit slit are properly selected, a monotonic response of the ratio of filtered-to-total Raman signal is obtained, as shown by the analytically calculated SFRS response curve in Fig. 41c. We have constructed a SFRS detection system as an addition to our Raman-microscope facility and are currently in the process of evaluating the SFRS instrument.
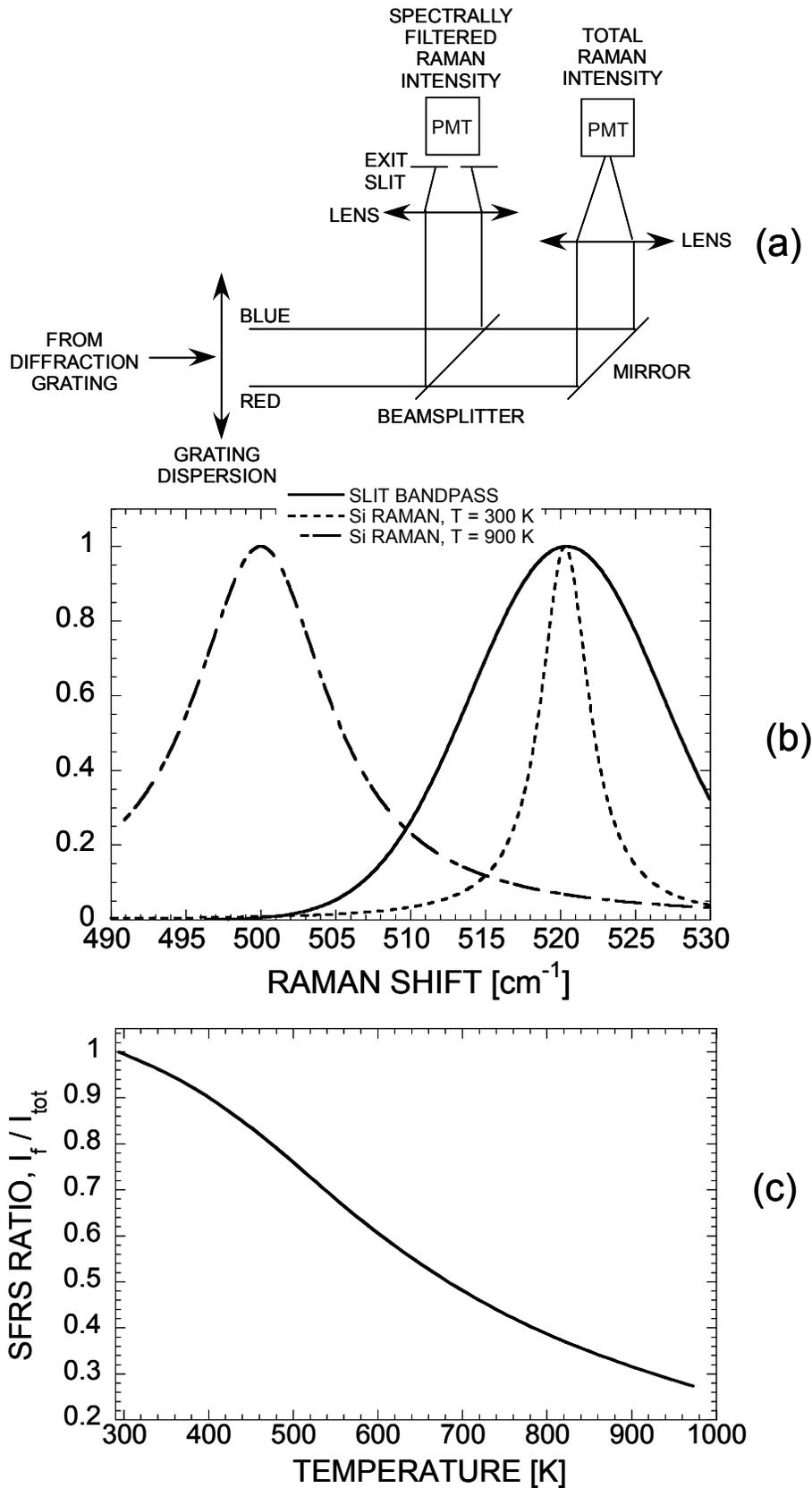
Figure 41 – Proposed Spectrally Filtered Raman Scattering (SFRS) diagnostic for fast Raman thermometry of MEMS devices. (a) SFRS optical detection scheme, which replaces the CCD camera of a conventional Raman microscope, (b) illustration of the relative spectral bandpass of the exit slit, a room-temperature Si Raman spectrum, and a Si Raman spectrum at 900 K, (c) comfuted temperature response of the ratio of filtered to unfiltered Si Raman signatures.

REFERENCES

1   O. Blum-Spahn, G. Grossetete, M. Polosky, D. Adams, C. C. Wong, F. Gass, R. Shul, M. Rightley, and D. Galdony, "Investigation of Optical Power Handling of a Surface Micromachined MEMS Shutter," SAND 2003-2475A; Sandia National Laboratories, Albuquerque, NM and Livermore, CA, 2003.

2   E. Sacks and J. Allen, "Configuration Space Representation for Micro-Mechanism Function*", *2nd International Conference on Engineering Design and Automation*; Maui, HI, 1998.

3   D. K. Serkland, K. M. Geib, G. M. Peake, G. R. Hadley, T. W. Hargett, A. T. Ongstad, V. M. Montano, G. A. Keeler, E. L. Blansett, T. M. Bauer, M. R. Medrano, and C. T. Sullivan, "Final Report on LDRD Project: Leaky-Mode VCSELs for Photonic Logic Circuits," SAND 2005-7118; Sandia National Laboratories, Albuquerque, NM and Livermore, CA, 2005.

4   M. S. Baker, R. A. Plass, T. J. Headley, and J. A. Walraven, "Final Report: Compliant Thermo-Mechanical MEMS Actuators LDRD #52553," SAND2004-6635; Sandia National Laboratories, Albuquerque, NM and Livermore, CA, 2004.

5   C. C. Wong, J. H. Flemming, and D. R. Adkins, "Evaluation of Mini/Micro-Pumps for Micro-Chem-Lab*", IMECE2002-33674, *ASME International Mechanical Engineering Congress and Exposition*; New Orleans, LA, 2002.

6   D. G. Cahill, K. E. Goodson, and A. Majumdar, "Thermometry and Thermal Transport in Micro/Nanoscale Solid-State Devices and Structures," *Journal of Heat Transfer* **124**, 223-241, 2002.

7   D. A. Fletcher, K. B. Crozier, C. F. Quate, G. S. Kino, and K. E. Goodson, "Near-Field Infrared Imaging with a Microfabricated Solid Immersion Lens," *Applied Physics Letters* **77**, 2109-2111, 2000.

8   M. Kuball, J. M. Hayes, M. J. Uren, T. Martin, J. C. H. Birbeck, R. S. Balmer, and B. T. Hughes, "Measurements of Temperature in Active High-Power AlGaN/GaN HFETs Using Raman Spectroscopy," *IEEE Electron Device Letters* **23**, 7-9, 2002.

9   R. Ostermeir, K. Brunner, G. Abstreiter, and W. Weber, "Temperature Distribution in Si-MOSFETs Studied by Micro Raman Spectroscopy," *IEEE Transactions on Electron Devices* **30**, 858-863, 1992.

10 M. N. Touzelbaev, P. Zhou, R. Venkatasubramanian, and K. E. Goodson, "Thermal Characterization of Bi_2Te_3/Sb_2Te_3 Superlattices," *Journal of Applied Physics* **90**, 763-767, 2001.

11 G. Hampel, P. Kolodner, P. L. Gammel, P. A. Polakos, E. de Obaldia, P. M. Mankiewich, A. Anderson, R. Slattery, D. Zhang, G. C. Liang, and C. F. Shih, "High Power Failure of Superconducting Microwave Filters: Investigation by Means of Thermal Imaging," *Applied Physics Letters* **69**, 571-573, 1996.

12 E. Anastassakis and E. Liarokapis, "Polycrystalline Si Under Strain: Elastic and Lattice Dynamical Considerations," *Journal of Applied Physics* **62**, 3346-3352, 1987.

13 I. DeWolf, "Micro-Raman Spectroscopy to Study Local Mechanical Stress in Silicon Integrated Circuits," *Semiconductor Science and Technology* **11**, 139-154, 1996.

14   G. Lucazeau, "Effect of Pressure and Temperature on Raman Spectra of Solids: Anharmonicity," *Journal of Raman Spectroscopy* **34**, 478-496, 2003.

15   T. R. Hart, R. L. Aggarwal, and B. Lax, "Temperature Dependence of Raman Scattering in Silicon," *Physical Review B* **1**, 638-642, 1970.

16   M. Balkanski, R. F. Wallis, and E. Haro, "Anharmonic Effects in Light Scattering Due to Optical Phonons in Silicon," *Physical Review B* **28**, 1928-1934, 1983.

17   R. Tsu and J. G. Hernandez, "Temperature Dependence of Silicon Raman Lines," *Applied Physics Letters* **41**, 1016-1018, 1982.

18   M. Bowden and D. J. Gardiner, "High Resolution Raman Shift and Bandwidth Images of Stressed Silicon," *Internet Journal of Vibrational Spectroscopy* **2**, 1998.

19   M. R. Abel, T. L. Wright, E. O. Sunden, S. Graham, and W. P. King, "Thermal Metrology of Silicon Microstructures using Raman Spectroscopy*", 21st IEEE SEMI-THERM Symposium*; San Jose, CA, 2005.

20   Y. S. Ju, *Microscale Heat Conduction in Integrated Circuits and Their Constituent Films*, Ph.D. Dissertation, Department of Mechanical Engineering; Stanford University, Stanford, CA, 1999.

21   W. Claeys, S. Dilhaire, V. Quintard, and J. P. Dom, "Absolute Dynamic Measurements of Temperature Changes in Electronic Components from a Thermoreflectance Optical Test Probe*", Third European Test Conference*; 378-384, 1993.

22   V. Quintard, G. Deboy, S. Dilhaire, D. Lewis, T. Phan, and W. Claeys, "Laser-Beam Thermography of Circuits in the Particular Case of Passivated Semiconductors," *Microelectronic Engineering* **31**, 291-298, 1996.

23   Y. S. Ju, O. W. Kading, Y. K. Leung, S. S. Wong, and K. E. Goodson, "Short-Timescale Thermal Mapping of Semiconductor Devices," *IEEE Electron Device Letters* **18**, 169-171, 1997.

24   G. Tessier, G. Jerosolimski, S. Hole, D. Fournier, and C. Filloy, "Measuring and Predicting the Thermoreflectance Sensitivity as a Function of Wavelength on Encapsulated Materials," *Review of Scientific Instruments* **74**, 495-499, 2003.

25   T. Juhasz, H. E. Elsayed-Ali, X. H. Hu, and W. E. Bron, "Time-Resolved Thermoreflectivity of Thin Gold Films and Its Dependence on the Ambient Temperature," *Physical Review B* **45**, 13819-13822, 1992.

26   X. Xu, C. P. Grigoropoulos, and R. E. Russo, "Transient Temperature During Pulsed Excimer Laser Heating of Thin Polysilicon Films Obtained by Optical Reflectivity Measurement," *Journal of Heat Transfer* **117**, 17-24, 1995.

27   J. Hohlfeld, J. G. Muller, S. S. Wellershoff, and E. Matthias, "Time-Resolved Thermoreflectivity of Thin Gold Films and its Dependence on Film Thickness," *Applied Physics B* **64**, 387-390, 1997.

28   A. C. Eckbreth, *Laser Diagnostics for Combustion Temperature and Species*: 2nd ed. Gordon and Breach, 1996.

29   H. M. Rosenberg, *The Solid State*: 3rd ed. Oxford University Press, 1988.

30   C. Kittel, *Introduction to Solid State Physics*: 7th ed. Wiley, 1996.

31   J. J. Sniegowski and M. P. de Boer, "IC-Compatible Polysilicon Surface Micromachining," *Annual Reviews of Materials Science* **30**, 299-333, 2000.

32   D. Bohm, *Quantum Theory*: Prentice-Hall, 1951.

33   D. J. Gardiner, M. Bowden, and P. R. Graves, "Novel Applications of Raman Microscopy," *Philosophical Transactions of the Royal Society of London A* **320**, 295-306, 1986.

34   J. H. Comtois and V. M. Bright, "Applications for Surface-Micromachined Polysilicon Thermal Actuators and Arrays," *Sensors and Actuators A* **58**, 19-25, 1997.

35   Q. A. Huang and N. K. S. Lee, "Analysis and Design of Polysilicon Thermal Flexure Actuator," *Journal of Micromechanics and Microengineering* **9**, 64-70, 1999.

36   R. Hickey, M. Kujath, and T. Hubbard, "Heat Transfer Analysis and Optimization of Two-Beam Microelectromechanical Thermal Actuators," *Journal of Vacuum Science and Technology A* **20**, 971-974, 2002.

37   C. D. Lott, T. W. McLain, J. N. Harb, and L. L. Howell, "Modeling the Thermal Behavior of a Surface-Micromachined Linear Displacement Thermomechanical Actuator," *Sensors and Actuators A* **101**, 239-250, 2002.

38   R. Hickey, D. Sameoto, T. Hubbard, and M. Kujath, "Time and Frequency Response of Two-Arm Micromachined Thermal Actuators," *Journal of Micromechanics and Microengineering* **13**, 40-46, 2003.

39   L. Li and D. Uttamchandani, "Modified Asymmetric Micro-Electrothermal Actuator: Analysis and Experimentation," *Journal of Micromechanics and Microengineering* **14**, 1734-1741, 2004.

40   S. P. Kearney, L. M. Phinney, and M. S. Baker, "Spatially Resolved Temperature Mapping of Electrothermal Actuators by Surface Raman Scattering," *Journal of Microelectromechanical Systems* **15**, 314-321, 2006.

41   J. R. Serrano, L. M. Phinney, and S. P. Kearney, "Micro-Raman Thermometry of Thermal Flexure Actuators," *Journal of Micromechanics and Microengineering* **16**, 1128-1134, 2006.

42   M. S. Baker, Personal Communication, 2005.

43   J. H. Comtois, M. A. Michalicek, and C. C. Barron, "Electrothermal Actuators Fabricated in Four-Level Planarized Surface Micromachined Polycrystalline Silicon," *Sensors and Actuators A* **70**, 23-31, 1998.

44   L. Que, J. S. Park, and Y. B. Gianchandani, "Bent-Beam Electrothermal Actuators – Part I: Single-Beam and Cascaded Devices," *Journal of Microelectromechanical Systems* **10**, 247-254, 2001.

45   L. L. Howell and S. M. Lyon, "Thermomechanical In-Plane Microactuator", US Patent no. 6,734,597; 2004.

46   H. Guckel, J. Klein, T. Christensen, K. Skrobis, M. Laundon, and E. G. Lovell, "Thermomagnetic Metal Flexure Actuators*", IEEE Solid State Sensor and Actuator Workshop*; 73-75, 1992.

47   J. H. Comtois, M. A. Michalicek, and C. C. Barron, "Characterization of Electrothermal Actuators and Arrays Fabricated in a Four-Level, Planarized Surface-Micromachined Polycrystalline Silicon Process*", International Conference on Solid-State Sensors and Actuators*; Chicago, IL, 769-772, 1997.

48   Q. A. Huang and N. K. S. Lee, "Analytical Modeling and Optimization for a Laterally Driven Polysilicon Thermal Actuator," *Microsystem Technologies* **5**, 133-137, 1999.

49 Y. Kuang, Q. A. Huang, and N. K. S. Lee, "Numerical Simulation of a Polysilicon Thermal Flexure Actuator," *Microsystem Technologies* **8**, 17-21, 2002.

50 J. Kim and L. Lin, "Electrostatic Scanning Micromirrors Using Localized Plastic Deformation of Silicon," *Journal of Micromechanics and Microengineering* **15**, 1777-1785, 2005.

51 R. A. Conant and R. S. Muller, "Cyclic Fatigue Testing of Surface Micromachined Thermal Actuators*", ASME International Mechanical Engineering Congress and Exposition*; Anaheim, CA, 273-277, 1998.

52 M. Kuball, S. Rajasingam, A. Sarua, M. J. Uren, T. Martin, B. T. Hughes, K. P. Hilton, and R. S. Balmer, "Measurement of Temperature Distribution in Multifinger AlGaN/GaN Heterostructure Field Effect Transistors Using Micro-Raman Spectroscopy," *Applied Physics Letters* **82**, 124-126, 2003.

53 J. C. Freeman, "Channel Temperature Model for Microwave AlGaN/GaN HEMTs on SiC and Sapphire MMICs in High Power, High Efficiency SSPAs," NASA TM 2004-212900; National Aeronautics and Space Administration, 2004.

54 S. L. Shinde, E. S. Piekos, T. A. Friedmann, and J. P. Sullivan, Personal Communication, 2005.

55 R. J. Moffat, "Describing the Uncertainties in Experimental Results," *Experimental Thermal Fluid Science* **1**, 3-17, 1988.

56 M. Kuball, "Raman Spectroscopy of GaN, AlGaN, and AlN for Process Growth and Monitoring/Control," *Surface and Interface Analysis* **31**, 987-999, 2001.

57 V. T. Srikar, A. K. Swan, M. S. Ünlü, B. B. Goldberg, and S. M. Spearing, "Micro-Raman Measurement of Bending Stresses in Micromachined Silicon Flexures," *Journal of Microelectromechanical Systems* **12**, 779-787, 2003.

58 S. Bergma, J. J. Gorman, and N. G. Dagalakis, "Design and Modeling of Thermally Actuated MEMS Nanopositioners*", IMECE2005-82158, ASME International Mechanical Engineering Congress and Exposition*; Orlando, FL, 2005.

59 R. Rosei and D. W. Lynch, "Thermomodulation Spectra of Al, Au, and Cu," *Physical Review B*, 3883-3894, 1972.

60 X. Xu and C. P. Grigoropoulos, "High Temperature Radiative Properties of Thin Polysilicon Films at the $\lambda = 0.6328$ μm Wavelength," *International Journal of Heat and Mass Transfer* **36**, 4163-4172, 1993.

61 J. Heller, J. W. Bartha, C. C. Poon, and A. C. Tam, "Temperature Dependence of the Reflectivity of Silicon with Surface Oxide at Wavelengths of 633 and 1047 nm," *Applied Physics Letters* **75**, 43-45, 1999.

62 D. E. Aspenes and A. A. Studna, "Dielectric Functions and Optical Parameters of Si, Ge, GaP, GaAs, GaSb, InP, InAs and InSb from 1.6 to 6.0 eV," *Physical Review B* **27**, 985-1009, 1983.

63 G. E. Jellison and F. A. Modine, "Optical Functions of Silicon Between 1.7 and 4.7 eV at Elevated Temperatures," *Physical Review B* **27**, 7466-7472, 1983.

64 B. K. Sun, X. Zhang, and C. P. Grigoropoulos, "Spectral Optical Functions of Silicon in the Range of 1.13-4.96 eV at Elevated Temperatures," *International Journal of Heat and Mass Transfer* **40**, 1591-1600, 1997.

65   G. Chen and C. L. Tien, "Internal Reflection Effects on Transient Photothermal Reflectance," *Journal of Applied Physics* **73**, 3461-3466, 1993.

66   J. R. Serrano, L. M. Phinney, and C. F. Brooks, "Laser-Induced Damage of Polycrystalline Silicon Optically Powered MEMS Actuators *"*, IPACK2005-73322, *ASME InterPACK2005*; San Francisco, CA, 2005.

67   L. M. Phinney and J. R. Serrano, "Optically Powered MEMS Actuators," *Sensors and Actuators A (in press)*, 2006.

68   D. E. Hare and D. D. Dlott, "Picosecond Coherent Raman Study of Solid-State Chemical Reactions During Laser Polymer Ablation," *Applied Physics Letters* **64**, 715-717, 1994.

69   S. V. Govorkov, N. I. Koroteev, I. L. Shumay, and V. N. Zadkov, "CARS Probing of the Si Raman Mode Transformation During Strong Picosecond Pulsed-Laser Irradiation," *Solid State Communications* **62**, 331-334, 1987.

70   J. Buhler and Y. Prior, "Back-Scattering CARS Diagnostics on CVD Diamond," *Diamond and Related Materials* **8**, 673-676, 1999.

71   S. P. Kearney, R. P. Lucht, and A. M. Jacobi, "Temperature Measurements in Convective Heat Transfer Flows using Dual-Broadband Pure-Rotational Coherent Anti-Stokes Raman Spectroscopy (CARS)," *Experimental Thermal Fluid Science* **19**, 13-26, 1999.

72   S. P. Kearney and M. N. Jackson, "Dual-Pump CARS Thermometry in Sooting Acetylene-Fueled Flames*"*, AIAA-2006-432, *44th AIAA Aerospace Sciences Meeting and Exhibit*; Reno, NV, 2006.

73   T. A. Reichardt, P. E. Schrader, and R. L. Farrow, "Comparison of Gas Temperatures Measured by Coherent Anti-Stokes Raman Spectroscopy (CARS) of O_2 and N_2," *Applied Optics* **40**, 741-747, 2001.

74   N. Hayazawa, M. Motohashi, Y. Saito, and S. Kawata, "Highly Sensitive Strain Detection in Strained Silicon by Surface-Enhanced Raman Spectroscopy," *Applied Physics Letters* **86**, 263114 1-3, 2005.

75   A. Campion and P. Kambhampati, "Surface-Enhanced Raman Scattering," *Chemical Society Reviews* **27**, 241-250, 1998.

76   S. P. Kearney, S. J. Beresh, R. W. Schefer, and T. W. Grasser, "Filtered Rayleigh Scattering Diagnostic for Multi-Parameter Thermal-Fluids Measurements: LDRD Final Report," SAND2004-0158; Sandia National Laboratories, Albuquerque, NM and Livermore, CA, 2004.

77   S. P. Kearney, R. W. Schefer, S. J. Beresh, and T. W. Grasser, "Temperature Imaging in Nonpremixed Flames by Joint Filtered Rayleigh and Raman Scattering," *Applied Optics* **44**, 1548-1558, 2005.

DISTRIBUTION

1	MS-0824	01500	T.Y.	Chu
1	MS-0384	01500	A.C.	Ratzel
1	MS-0824	01510	W.L.	Hermina
1	MS-0834	01512	C.F.	Brooks
8	MS-0834	01512	S.P.	Kearney
1	MS-0834	01512	R.D.M.	Tachau
1	MS-0834	01512	W.M.	Trott
1	MS-0834	01512	S.M.	Trujillo
1	MS-0834	01513	C.J.	Bourdon
1	MS-0826	01513	M.A.	Gallis
1	MS-0826	01513	A.S.	Geller
1	MS-0834	01513	A.M.	Grillet
5	MS-0834	01513	L.M.	Phinney
1	MS-0826	01513	E.S.	Piekos
1	MS-0825	01513	D.J.	Rader
5	MS-0834	01513	J.R.	Serrano
1	MS-0826	01513	J.R.	Torczynski
1	MS-0826	01513	C.C.	Wong
1	MS-0836	01514	J.S.	Lash
1	MS-0825	01515	B.	Hassan
1	MS-0836	01516	E.S.	Hertel
1	MS-0836	01517	R.O.	Griffith
1	MS-0847	01520	P.J.	Wilson
1	MS-0847	01526	J.M.	Redmond
1	MS-0821	01530	A.L.	Thornton
1	MS-0380	01540	H.S.	Morgan
1	MS-1423	01128	G.A.	Hebner
1	MS-0792	01715-2	M.J.	Rightley
1	MS-1081	01726	R.E.	Anderson
1	MS-1082	01727	I.	Brener
1	MS-1082	01727	F.B.	McCormick
1	MS-1082	01727	W.C.	Sweatt
1	MS-1077	01740	T.E.	Zipperian
1	MS-1085	01742	A.G.	Baca
1	MS-1085	01742	C.T.	Sullivan
1	MS-1080	01749	D.R.	Sandison
1	MS-1069	01749-1	M.S.	Baker
1	MS-1069	01749-1	M.R.	Platzbecker
1	MS-1069	01749-1	D.M.	Tanner
1	MS-0885	01810	J.E.	Johannes
1	MS-0889	01824	B.L.	Boyce
1	MS-1064	02455	J.A.	Palmer
1	MS-0613	02520	M.R.	Prairie
1	MS-1064	02614	S.E.	Lott
1	MS-0529	05350	S.C.	Holswade
1	MS-1243	05535	S.N.	Kempka
2	MS-9018	08944	Central Technical Files	
2	MS-0899	04536	Technical Library	

External

3   Professor Samuel Graham
     G.W. Woodruff School of Mechanical
     Engineering
     Georgia Institute of Technology
     771 Ferst Drive
     Atlanta, GA 30332-0405